LJMU Research Online

Barber, C, Schaye, J and Crain, RA

 Calibrated, cosmological hydrodynamical simulations with variable IMFs III: spatially resolved properties and evolution

http://researchonline.ljmu.ac.uk/id/eprint/10522/

Article

For more information please contact researchonline@ljmu.ac.uk

Calibrated, cosmological hydrodynamical simulations with variable IMFs III: spatially resolved properties and evolution

Christopher Barber,[1]⋆ Joop Schaye [1] and Robert A. Crain [2]

[1]*Leiden Observatory, Leiden University, PO Box 9513, NL-2300 RA Leiden, The Netherlands*
[2]*Astrophysics Research Institute, Liverpool John Moores University, 146 Brownlow Hill, Liverpool L3 5RF, UK*

ABSTRACT

Recent spatially resolved observations of massive early-type galaxies (ETGs) have uncovered evidence for radial gradients of the stellar initial mass function (IMF), ranging from super-Salpeter IMFs in the centre to Milky Way-like beyond the half-light radius, r_e. We compare these findings with our new cosmological, hydrodynamical simulations based on the Evolution and Assembly of GaLaxies and their Environments (EAGLE) model that self-consistently vary the IMF on a per-particle basis such that it becomes either bottom-heavy (LoM-50) or top-heavy (HiM-50) in high-pressure environments. These simulations were calibrated to reproduce inferred IMF variations such that the IMF becomes 'heavier' due to either excess dwarf stars or stellar remnants, respectively, in galaxies with increasing stellar velocity dispersion. In agreement with observations, both simulations produce negative radial IMF gradients, transitioning from high to low excess mass-to-light ratio (MLE) at around r_e. We find negative metallicity radial gradients for both simulations, but positive and flat [Mg/Fe] gradients in LoM-50 and HiM-50, respectively. Measured in radial bins, the MLE increases strongly with local metallicity for both simulations, in agreement with observations. However, the local MLE increases and decreases with local [Mg/Fe] in LoM-50 and HiM-50, respectively. These qualitative differences can be used to break degeneracies in the manner with which the IMF varies in these high-mass ETGs. At $z = 2$, we find that the MLE has a higher and lower normalization for bottom- and top-heavy IMF variations, respectively. We speculate that a hybrid of our LoM and HiM models may be able to reconcile observed IMF diagnostics in star-forming galaxies and ETGs.

Key words: methods: numerical – stars: luminosity function, mass function – galaxies: elliptical and lenticular, cD – galaxies: evolution – galaxies: fundamental parameters – galaxies: structure.

1 INTRODUCTION

How early-type galaxies (ETGs) form and evolve over cosmic time is an area of active research, where one of the leading theories invokes an 'inside–out' formation scenario that occurs in two distinct phases (Bezanson et al. 2009; Oser et al. 2010; Barro et al. 2013; Clauwens et al. 2018). First, the dense stellar core is formed at high redshift, in a rapid, high-pressure burst of star formation. In the second phase, stellar mass is accreted through minor and major mergers with other galaxies, adding material to the outer regions of ETGs. The different physical conditions under which the stars form in each of these phases gives rise to gradients in stellar properties as a function of radius (Mehlert et al. 2003; Kuntschner et al. 2010; Greene et al. 2015).

Equipped with the spatial and spectral resolving power of modern, panoramic integral field units, observational studies have recently inferred that the stellar initial mass function (IMF) varies radially in the centres of some local high-mass ETGs. In general, such studies conclude that the IMF is bottom heavy in galaxy centres due to an excess of dwarf stars, transitioning to an IMF consistent with a Kroupa (i.e. Milky-Way-like) IMF from ≈0.1 to 1 times the half-light radius, r_e (Boroson & Thompson 1991; Martín-Navarro et al. 2015b; La Barbera et al. 2016; van Dokkum et al. 2017; Sarzi et al. 2018; Oldham & Auger 2018a). The presence of such gradients is still energetically debated, however, with some studies finding no gradients or arguing that it is currently too difficult to disentangle the IMF from radial abundance gradients (McConnell, Lu & Mann 2016; Zieleniewski et al. 2017; Davis & McDermid 2017; Alton, Smith & Lucey 2017, 2018; Vaughan et al. 2018a,b).

Such findings are important, since the IMF is usually assumed to be universal, both in the interpretation of observations and when

⋆ E-mail: cbar@strw.leidenuniv.nl

making predictions with galaxy formation models. For example, radial IMF gradients imply that the stellar mass-to-light (M/L) ratio in these galaxies varies as a function of radius, which could have a strong impact on dynamical mass models in which it is typically assumed that the M/L ratios measured in the central regions of galaxies apply globally (see Bernardi et al. 2018; Sonnenfeld et al. 2018; Oldham & Auger 2018b). Indeed, radial IMF variations may affect measurements of the IMF itself when inferring it within some fixed aperture.

Understanding how the IMF varies within a galaxy can give insights into the nature of the variation itself, both in terms of the physical origin of the variations, as well which part of the IMF is varying, and in which direction. For example, Martín-Navarro et al. (2015c) concluded that the spatially resolved IMF correlates with local metallicity in 24 high-mass ETGs from the Calar Alto Legacy Integral Field Area (CALIFA) survey, which could imply that metallicity may play an important role in shaping the IMF. This result is qualitatively consistent with the recent findings of van Dokkum et al. (2017) for six high-mass ETGs. Interestingly, these two studies assume very different parametrizations of IMF variations, steepening the low- and high-mass IMF slopes, respectively. Since most metals are produced by high-mass stars, the parametrization of the IMF variations is crucial to the predictions of galaxy formation models that attempt to invoke such IMF variations. For instance, if the high-mass slope correlates with metallicity, it is not clear if such correlations are due to a causation in either direction or a coincidence, since both quantities also scale strongly with radius.

That present-day high-mass ETGs formed the majority of their stars at high redshift leads to questions concerning how the IMF may have evolved over time. Indeed, observations of strongly star-forming galaxies at high redshift conclude that the high-mass slope of the IMF may need to be shallower to account for their Hα equivalent widths (EWs, Nanayakkara et al. 2017) or abundance ratios (Zhang et al. 2018). On the other hand, observations of present-day high-mass ETGs, which are the descendants of high-redshift starbursts, are typically found to have bottom-heavy stellar populations, with their stellar spectra indicating an excess of dwarf stars relative to a Milky Way-like IMF (e.g. Conroy & van Dokkum 2012; La Barbera et al. 2013). These apparently contradictory results could be evidence of a time dependence of IMF variations. Indeed, different forms of IMF parametrization can lead to very different predictions of IMF-related observational diagnostics at the present day, even for a fixed M/L ratio (Barber, Crain & Schaye 2018a, hereafter Paper I). These differences may be even stronger at high redshift when the stars are actually forming.

Such issues can be addressed with galaxy formation models that explicitly include IMF variations. The recent cosmological, hydrodynamical simulations of Paper I are currently the most well suited to answer these questions. The IMF variations in these simulations were assumed to depend on the local pressure of star-forming gas and were calibrated to reproduce the correlation between galaxy-wide mass-to-light excess (MLE) and central stellar velocity dispersion, σ_e, inferred by Cappellari et al. (2013b). This match was achieved by increasing the contribution of either low-mass dwarf stars or stellar remnants [black holes (BHs), neutron stars (NSs), and white dwarfs] to the stellar M/L by varying the low- or high-mass IMF slope, respectively, to become bottom- or top heavy in high-pressure environments on a per-particle basis. The IMF variations in these simulations are fully self-consistent in terms of the local star formation law, stellar energetic feedback, and nucleosynthetic yields.

We showed in Paper I that these simulations, which employ the Evolution and Assembly of GaLaxies and their Environments (EAGLE) model for galaxy formation (Schaye et al. 2015), agree with the observables used to calibrate this model, namely the present-day galaxy luminosity function, half-light radii, and supermassive BH masses. In Barber, Schaye & Crain (2018b, hereafter Paper II), we investigated correlations between the 'galaxy-wide' IMF and galaxy properties at $z = 0.1$, including metallicity, [Mg/Fe], age, stellar mass, luminosity, size, and BH mass. In this paper, the third in this series, we use our variable IMF simulations (summarized in Section 2) to investigate if radial IMF gradients, which were not considered in the initial IMF calibrations, are predicted by our models (Section 3.2), and see how plausible IMF variations may affect radial gradients in stellar population properties such as the M/L ratio, metallicities, and α-enhancement (Section 3.3). We also investigate how the local IMF varies with local properties, and directly compare with recent observations (Section 3.4). In Section 4, we investigate the evolution of the IMF and its effect on the evolution of galaxies in the simulations. We discuss our models and possible extensions in Section 5. Finally, we present our conclusions in Section 6. The simulation data are publicly available at http://icc.dur.ac.uk/Eagle/database.php (McAlpine et al. 2016).

2 SIMULATIONS

The simulations used in this work are a variation on the EAGLE project, a suite of cosmological, hydrodynamical simulations of galaxy formation and evolution (Schaye et al. 2015; Crain et al. 2015; McAlpine et al. 2016). They were run using the Tree-Particle-mesh smooth particle hydrodynamics code P-GADGET-3 (last described by Springel 2005) in a periodic, comoving volume of (50 Mpc)^3 from $z = 127$ to 0. They have the same resolution as the fiducial EAGLE model, with particle mass of $m_g = 1.8 \times 10^6$ M$_\odot$ and $m_{DM} = 9.7 \times 10^6$ M$_\odot$ for gas and dark matter, respectively. The gravitational softening length was set to 2.66 comoving kpc for $z > 2.8$ and held fixed at 0.70 proper kpc thereafter. A Λ cold dark matter cosmogony is assumed, with cosmological parameters chosen for consistency with *Planck* 2013 ($\Omega_b = 0.04825$, $\Omega_m = 0.307$, $\Omega_\Lambda = 0.693$, and $h = 0.6777$; Planck Collaboration 2014).

In the reference EAGLE model, physical processes that occur below the resolution limit of the simulation are modelled via 'sub-grid' prescriptions. Gas particles cool radiatively according to cooling rates determined for the 11 individually tracked elements that are most important for cooling (Wiersma, Schaye & Smith 2009a), and are photoheated by an evolving, spatially uniform (Haardt & Madau 2001) ultraviolet (UV)/X-ray background and the cosmic microwave background. When gas particles become sufficiently dense and cool (Schaye 2004), they become eligible to stochastically transform into star particles. These star particles evolve and lose mass via supernovae (SNe) type Ia and II, and winds from asymptotic giant branch stars and massive stars (Wiersma et al. 2009b) according to an IMF (which in the reference EAGLE model is assumed to universally follow a Chabrier 2003 form) and metallicity-dependent lifetimes of Portinari, Chiosi & Bressan (1997). Thermal stellar feedback is implemented stochastically (Dalla Vecchia & Schaye 2012) and was calibrated to match the $z \approx 0$ galaxy stellar mass function and galaxy sizes. Supermassive BHs are seeded in high-mass haloes and can grow via BH–BH mergers or gas accretion (Springel, Di Matteo & Hernquist 2005; Booth & Schaye 2009; Rosas-Guevara et al. 2015), the latter leading to thermal active galactic nucleus (AGN) feedback that quenches star formation in high-mass galaxies. We refer the reader to Schaye et al. (2015)

for a more detailed description of the EAGLE model and to Crain et al. (2015) for details of its calibration.

The models employed in our two variable IMF simulations (first presented in Paper I) differ from the reference EAGLE model in that, rather than assuming a fixed Chabrier IMF for all stellar populations, they self-consistently vary the IMF for individual star particles as a function of the pressure of the interstellar medium (ISM) in which each star particle forms.[1] The IMF is defined over the range $0.1 - 100\,\mathrm{M_\odot}$ with a mass-dependent slope $x(m)$ as $\mathrm{d}n/\mathrm{d}m \propto m^{x(m)}$. The two IMF variation prescriptions studied are shown in Fig. 1. The left-hand panel shows the model termed 'LoM', where the IMF transitions from bottom light to bottom heavy from low to high pressures by varying the low-mass ($m < 0.5\,\mathrm{M_\odot}$) slope of the IMF while keeping the high-mass slope fixed at the Kroupa value of $x = -2.3$. For the second prescription, called 'HiM' (right-hand panel), we instead vary the high-mass slope ($m > 0.5\,\mathrm{M_\odot}$) to transition from Kroupa-like to top heavy from low to high pressures while keeping the low-mass slope fixed at the Kroupa value of $x = -1.3$. Due to the finite resolution of EAGLE, this pressure corresponds to the ISM pressure averaged on scales of $\approx 1\,\mathrm{kpc}$. Note that for a self-gravitating disc, variations with pressure are equivalent to variations with star formation rate (SFR) surface density (Schaye & Dalla Vecchia 2008). Crucially, both IMF variation prescriptions were calibrated to broadly reproduce the correlation between the MLE relative to that expected given a fixed IMF, and central stellar velocity dispersion, σ_e, inferred for high-mass ETGs by Cappellari et al. (2013b). Stellar feedback, the star formation law, and metal yields were all modified to self-consistently account for the local IMF variations. We refer the reader to Paper I for further details of these IMF prescriptions and their calibration.

Since the simulations do not explicitly model the emission of optical light, we compute photometric luminosities for all stellar particles (in post-processing) using the flexible stellar population synthesis (FSPS) software package (Conroy, Gunn & White 2009; Conroy & Gunn 2010), using the Basel spectral library (Lejeune, Cuisinier & Buser 1997, 1998; Westera et al. 2002) with Padova isochrones (Marigo & Girardi 2007; Marigo et al. 2008), where the stellar population's age, metallicity, initial stellar mass, and IMF are all taken into account. For consistency, we also recompute stellar masses using FSPS, and note that for the highest mass ($M_\star > 10^{11}\,\mathrm{M_\odot}$) galaxies in HiM-50 this leads to larger stellar masses of up to 0.2 dex due to differences in how stellar remnants are computed in FSPS and the Wiersma et al. (2009b) model built into EAGLE. We assume that stellar populations with age < 10 Myr have zero luminosity since such populations are expected to be obscured by their birth clouds (Charlot & Fall 2000), but otherwise account for no further effects of dust.

Galaxies are identified in the simulations using a friends-of-friends halo finder combined with the SUBFIND algorithm which identifies self-bound structures (Springel et al. 2001; Dolag et al. 2009). We ensure that all galaxies studied in this work are well sampled, with each containing at least 500 bound stellar particles. Unless otherwise stated, we compute global galaxy properties such as the stellar velocity dispersion, σ_e, as a Sloan Digital Sky Survey (SDSS) r-band light-weighted average over all bound star particles

---

[1] We note also that on kpc scales, the pressure correlates well with the SFR surface density through the Kennicutt–Schmidt law (e.g. Schaye & Dalla Vecchia 2008), so our IMF prescription can also be interpreted as implementing a dependence of the IMF on other variables such as the radiation or cosmic ray density.

---

within the 2D projected r-band half-light radius, r_e, of each galaxy, where the projection is along the 'random' z-axis of the simulation.

In the upper row of Fig. 2, we show random projections of three example galaxies taken from LoM-50 at $z = 0.1$ with $\sigma_e \approx 60$, 100, and $> 150\,\mathrm{km\,s^{-1}}$. The grey-scale background shows projected stellar mass density maps, while coloured contours show maps of the mass-weighted low-mass ($m < 0.5\,\mathrm{M_\odot}$) IMF slope. For the high-σ_e galaxies, we see strong radial gradients of the IMF slope, starting as Chabrier-like in the outskirts and becoming more bottom heavy towards the centre. Some lower σ_e galaxies also show IMF gradients, but these are much weaker than those with higher σ_e. Analogously, in the lower row of Fig. 2, we show the same but for the HiM-50 simulation (with a different set of galaxies). Here, we also see strong radial gradients in the highest σ_e galaxies, but now the IMF becomes more top heavy toward the centre.

We show these trends statistically in Fig. 3, where in the upper and lower panels we plot respectively for LoM-50 and HiM-50, the radial profiles of the median IMF slope over the region of the IMF that is varied for star particles belonging to subhaloes in bins of σ_e. We see here that while high-σ_e galaxies ($\sigma_e > 125\,\mathrm{km\,s^{-1}}$) have strong radial IMF gradients, low-σ_e galaxies ($30 < \sigma_e/\mathrm{km\,s^{-1}} < 50$) have relatively flat profiles, remaining Kroupa-like at all radii. In the next section, we explore these radial trends in high-σ_e galaxies in detail and compare with observations.

3 IMF TRENDS WITHIN GALAXIES

In this section, we present the spatially resolved properties of high-σ_e galaxies in our variable IMF simulations. Section 3.1 describes the sample of high-mass ETGs selected for comparison with observations, for which we investigate radial gradients in the IMF and some of its observational diagnostics in Section 3.2. Section 3.3 shows the effect of IMF variations on gradients in stellar properties, and in Section 3.4, we present the resulting correlations between the local IMF and stellar properties within individual galaxies.

3.1 Sample selection

In order to compare the internal properties of galaxies in our variable IMF simulations with observations, we select ETGs with $\sigma_e > 150\,\mathrm{km\,s^{-1}}$, hereafter referred to as the 'Sigma150' sample. As in Papers I and II, we define ETGs as those with intrinsic (dust-free) $u^* - r^* > 2$. The σ_e limit of $150\,\mathrm{km\,s^{-1}}$ was chosen as a compromise between having a statistically significant number of galaxies in our sample and fairness of comparison with observational samples of high-σ galaxies. This selection leaves us with 40 and 5 Sigma150 galaxies in LoM-50 and HiM-50, respectively. The difference in sample sizes is due to a combination of lower typical σ_e values and lower passive fractions in HiM-50 galaxies (see Paper I). Note that selecting all galaxies with $\sigma_e > 150\,\mathrm{km\,s^{-1}}$ rather than only ETGs would increase our sample sizes for LoM-50 and HiM-50 to 67 and 12, respectively, but would make no qualitative difference to any of the results presented in this paper.

Fig. 4 shows r_e as a function of σ_e for our simulated ETGs, and compares with various observed high-σ ETGs that have spatially resolved IMF measurements. These observed samples will be described in Section 3.2. Our Sigma150 galaxies are slightly larger and have lower σ_e on average compared to the observational sample. However, note that for three of the observed galaxies from van Dokkum et al. (2017), including the smallest one, r_e is measured along the projected semiminor axis, which may be smaller than our (circularly averaged) r_e values. These differences should be kept in
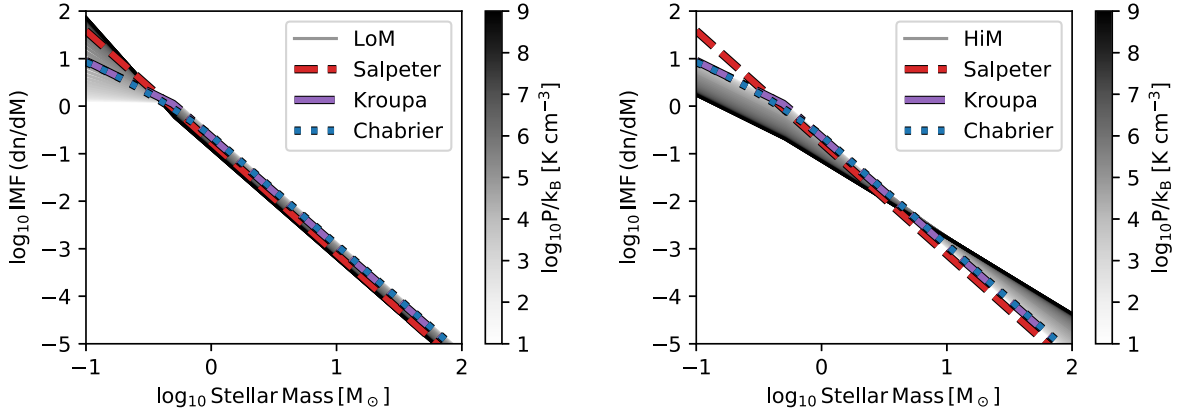
Figure 1. IMF variation prescriptions employed by LoM-50 (left-hand panel) and HiM-50 (right-hand panel). Grey lines show the IMF assigned to stellar populations for a range in birth ISM pressures (see grey-scale bar). For all IMFs, the integrated mass is normalized to $1\,M_\odot$. In LoM-50, the low-mass ($m < 0.5\,M_\odot$) IMF slope is varied such that the IMF transitions from bottom light to bottom heavy from low- to high-pressure environments. In HiM-50, the high-mass ($m > 0.5\,M_\odot$) IMF slope is instead varied to become top heavy in high-pressure environments. Figure reproduced from fig. 2 of Paper I.
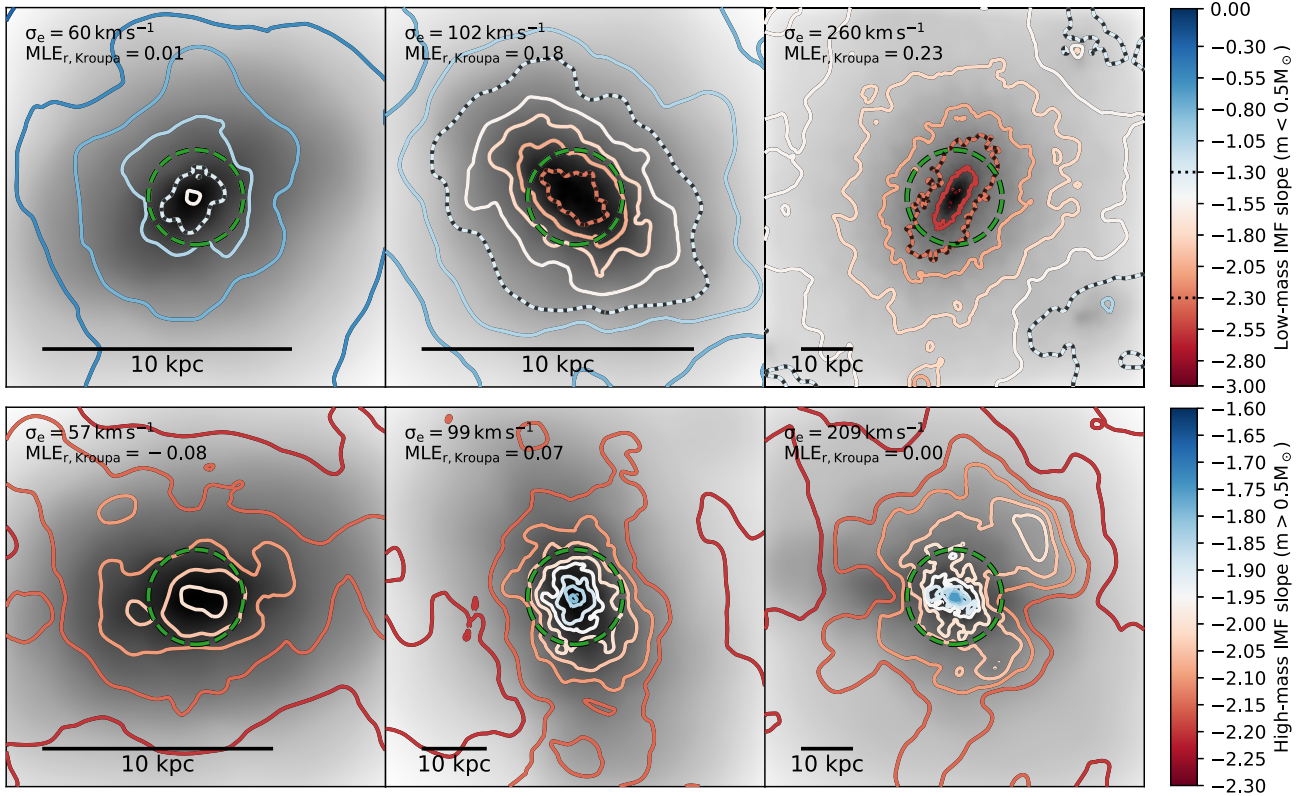
Figure 2. IMF maps for three example galaxies of different masses from each of LoM-50 (top row) and HiM-50 (bottom row) at $z = 0.1$. Grey-scale maps show logarithmic projected stellar mass surface density. The extent of each image is eight times the 2D projected SDSS r-band half-light radii, r_e, which is marked by a dashed green circle in each panel. Physical proper kpc are indicated with scale bars. Coloured contours (corresponding to ticks in the colour bars) denote mass-weighted IMF slope for $m < 0.5\,M_\odot$ (top row) and $m > 0.5\,M_\odot$ (bottom row). Bluer and redder colours correspond to shallower and steeper IMF slopes, respectively. In the upper row, we highlight the low-mass IMF slope contours corresponding to Kroupa and Salpeter IMFs as dotted white and red lines, respectively, where applicable. The stellar velocity dispersion, σ_e, and excess mass-to-light ratio relative to a Kroupa IMF ($MLE_{r,Kroupa}$, equation 1), both r band weighted and measured within r_e, are indicated in the upper left corner of each panel. Note that the upper and lower rows do not correspond to the same galaxies. LoM-50 (HiM-50) galaxies with higher σ_e tend to have more bottom-heavy (top-heavy) IMFs in their central regions, with steep gradients of increasing heaviness toward their centres. Lower mass galaxies have Chabrier-like IMFs and weaker IMF gradients.
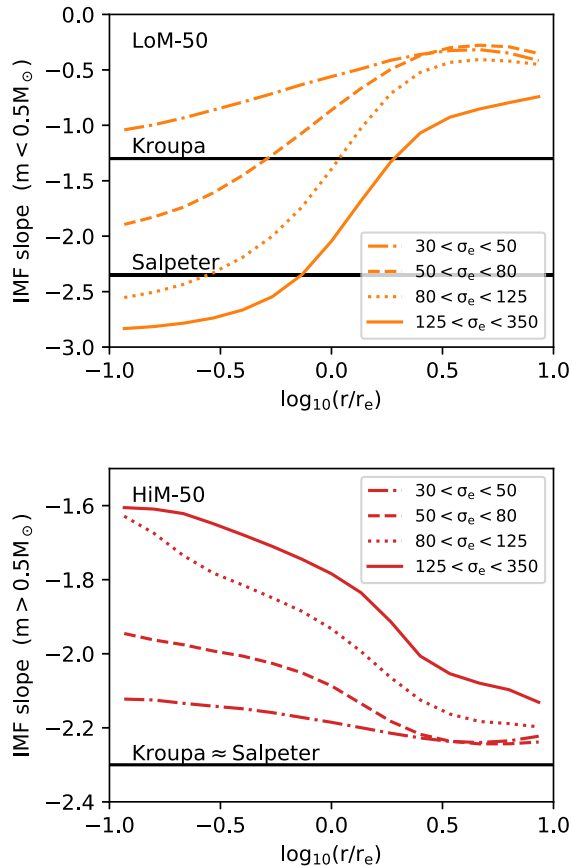
Figure 3. IMF slope as a function of 2D projected galactocentric radius at $z = 0.1$, normalized to the half-light radius of each galaxy. Coloured lines show median values for all stars belonging to subhaloes with stellar velocity dispersion, σ_e, in bins defined by the legend (in units of km s^{-1}). The upper panel shows the low-mass ($m < 0.5\,M_\odot$) slope for LoM-50 galaxies, while the lower panel shows the high-mass ($m > 0.5\,M_\odot$) slope for HiM-50 galaxies. IMF slopes for Salpeter and Kroupa IMFs are indicated with horizontal solid lines. In both simulations, IMF gradients are stronger in higher σ_e galaxies.

mind when comparing IMF diagnostics with observed galaxies in future sections.

3.2 Radial IMF gradients

To measure the radial dependence of the IMF within our galaxies, it is important to account for the non-circularity of the galaxy surface brightness profiles (see Fig. 2), as is also done in observational studies (e.g. Parikh et al. 2018). To do so, we fit an ellipse, with semimajor axis[2] equal to the circularly averaged r_e, to the 2D projected surface brightness profile of each galaxy. We then measure the r-band light-weighted IMF slope for each galaxy within concentric elliptical shells by scaling this ellipse such that its semimajor axis is logarithmically spaced in bins of width 0.1 dex, ranging from $\log_{10} r/r_e = -1$ to 1. We caution that, given the gravitational

---

[2]This choice is motivated by some observational IMF studies that measure r_e along the semimajor axis of the galaxy (e.g. Martín-Navarro et al. 2015d; van Dokkum et al. 2017). For ETGs, the difference between the circularly averaged r_e and the r_e measured along the semimajor axis is usually small, around 0.1 dex (see table 1 of Cappellari et al. 2013a), so this choice has little impact on our results.
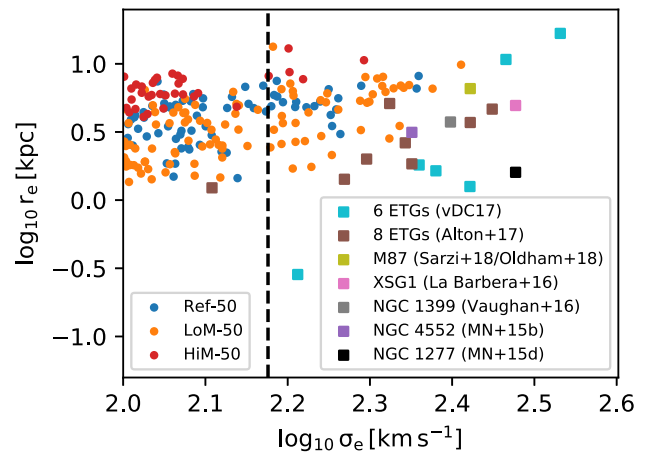
Figure 4. Projected proper r-band half-light radius, r_e, as a function of projected r-band light-weighted stellar velocity dispersion measured within r_e, σ_e, for ETGs (defined as those with intrinsic $u^* - r^* > 2$) in Ref-50 (dark blue dots), LoM-50 (orange dots), and HiM-50 (red dots) at $z = 0.1$. We compare with observed ETGs with recently measured spatially resolved IMFs shown as squares: the six high-σ_e ETGs studied by van Dokkum et al. (2017) in cyan, eight ETGs studied by Alton et al. (2017) in brown, M87 in yellow (studied separately by Sarzi et al. 2018; Oldham & Auger 2018a), XSG1 in pink (La Barbera et al. 2016), NGC 1399 in grey (Vaughan et al. 2018b), NGC 4552 in purple (Martín-Navarro et al. 2015b), and NGC 1277 in black (Martín-Navarro et al. 2015d, values from van den Bosch et al. 2012). Where possible, distances were taken from Cappellari et al. (2011) and σ_e and r_e from the above-mentioned references or Cappellari et al. (2013a). For each simulation, we select ETGs with $\sigma_e > 150\,\mathrm{km\,s^{-1}}$ (hereafter the 'Sigma150' sample) for comparison with observations, indicated by the vertical dashed line. Our Sigma150 galaxies have on average lower σ_e than the observed samples, which should be kept in mind when comparing our results with observations.

softening length of 0.7 kpc and that r_e for most of our galaxies lies in the range 2–10 kpc, any radial gradients at $r \lesssim 0.1 - 0.3\,r_e$ are likely affected by numerical resolution or the equation of state imposed on star-forming gas in EAGLE (Benítez-Llambay et al. 2018). Therefore, we show radial profiles only for $r > 0.1\,r_e$. Additionally, radii larger than $10\,r_e$ would be well beyond what can be measured observationally. Indeed, due to the fact that spectroscopic IMF studies require a signal-to-noise ratio (S/N) of at least 100 to detect variations in the dwarf-to-giant ratio, most such studies measure the IMF within, at most, a couple of r_e (e.g. Vaughan et al. 2018a).

In this section, we explore radial gradients for various IMF-dependent diagnostics, including the IMF slope (Section 3.2.1), MLE (Section 3.2.2), and the dwarf-to-giant ratio (Section 3.2.3).

3.2.1 IMF slope radial gradients

Fig. 5 shows the IMF slope as a function of r/r_e for our Sigma150 samples in LoM-50 and HiM-50 at $z = 0.1$, where we show the (varying) low- and high-mass slopes for the respective simulations. For both simulations, we see strong radial gradients, with the IMF becoming bottom and top heavy toward the centre for LoM-50 and HiM-50, respectively.

We compare our LoM-50 simulation with observed gradients in the low-mass IMF slope ($m < 0.5\,M_\odot$) inferred by Parikh et al. (2018) from NaI absorption features in the radially binned stacked spectra of 122 morphologically selected ETGs from the
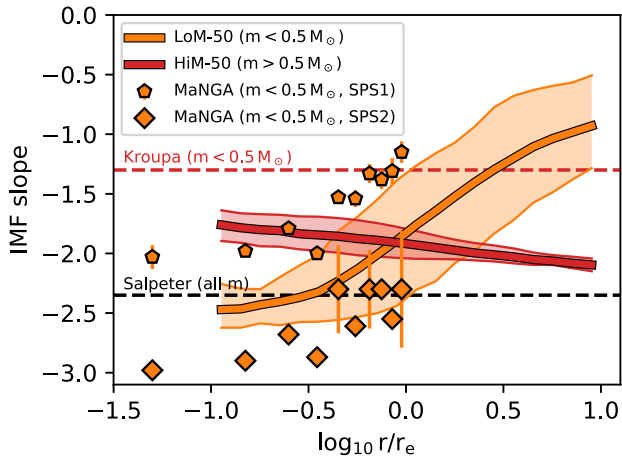
Figure 5. Radial variations in the *r*-band light-weighted IMF slope for ETGs with $\sigma_e > 150\,\mathrm{km\,s^{-1}}$ in the LoM-50 (orange) and HiM-50 (red) simulations at $z = 0.1$. We show only the slope for the mass range of the IMF that is varying: $m < 0.5\,\mathrm{M_\odot}$ and $m > 0.5\,\mathrm{M_\odot}$ for LoM-50 and HiM-50, respectively. Solid thick lines show mean values averaged over all galaxies within logarithmically binned 2D concentric elliptical shells with semimajor axis r/r_e, while solid filled regions show 10–90th percentiles. The dashed red line marks the low-mass slope for a Kroupa IMF (which is also the low-mass slope for all galaxies in HiM-50), while the black dashed line marks the Salpeter slope at all masses. We compare LoM-50 with low-mass slope variations for 122 ETGs in the mass range $\log_{10} M_\star/\mathrm{M_\odot} \in [10.5, 10.8]$ from SDSS–MaNGA as orange points where pentagons and diamonds correspond to differences in SPS modelling (Parikh et al. 2018). In both simulations, we find strong radial IMF gradients, with the IMF becoming more bottom and top heavy toward the centres of galaxies for LoM-50 and HiM-50, respectively. Our low-mass slope variations in LoM-50 agree well with observations within the errors associated with SPS modelling.

SDSS-IV Mapping Nearby Galaxies at APO (MaNGA) survey with $\log_{10} M_\star/\mathrm{M_\odot} \in [10.5, 10.8]$. To demonstrate the systematic uncertainty in the determination of the IMF slope via spectroscopic modelling, we show their results using two different stellar population synthesis (SPS) models: SPS1 uses the stellar population models of optical Lick absorption indices of Thomas, Maraston & Johansson (2011) in combination with Maraston & Strömbäck (2011) models based on the theoretical MARCS (Gustafsson et al. 2008) library, while SPS2 uses the Villaume et al. (2017) extended NASA Infrared Telescope Facility stellar library. While both models yield significant radial gradients in the IMF slope, they are significantly offset from one another. Encouragingly, they seem to straddle our LoM-50 results, making the agreement between our simulations and these observations very good within the systematic uncertainties of the SPS modelling.

Note that HiM-50, which by construction has a low-mass slope fixed at the Kroupa value (dashed red line in Fig. 5), is not consistent with these observations. Indeed, observational SPS studies that parametrize IMF variations by varying the high-mass IMF slope typically find that it becomes steeper toward the centre (e.g. Martín-Navarro et al. 2015b; La Barbera et al. 2016), which is also in conflict with the HiM-50 simulation. However, such studies are only sensitive to the low-mass end of the IMF, since only the long-lived stars (with $m \lesssim 1\,\mathrm{M_\odot}$) remain present in the old ETGs that are the focus of these IMF studies. Studies that are sensitive to the high-mass end of the IMF (e.g. Gunawardhana et al. 2011) and which inspired our HiM IMF variation prescription, have not yet explored radial gradients of the high-mass slope within galaxies. It will thus be an
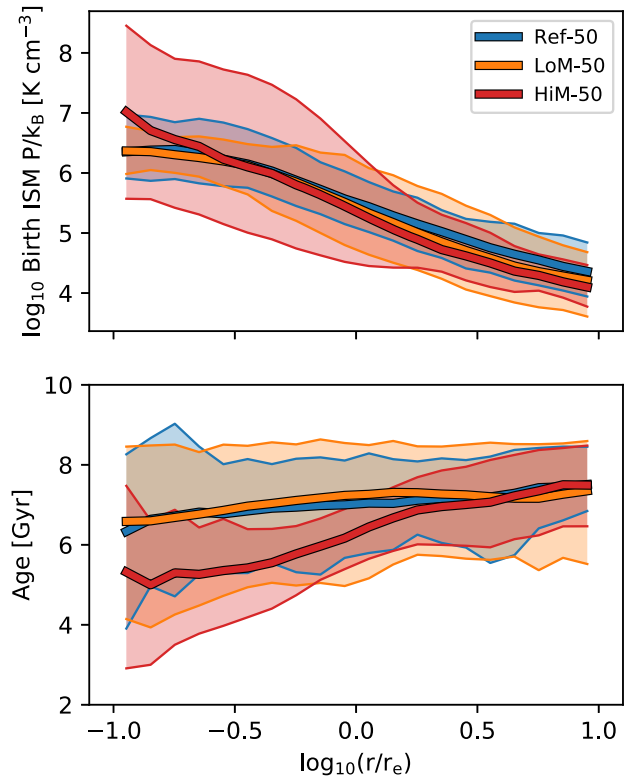
Figure 6. Radial variations of spatially resolved properties of ETGs with $\sigma_e > 150\,\mathrm{km\,s^{-1}}$ in Ref-50 (blue), LoM-50 (orange), and HiM-50 (red) at $z = 0.1$. We show *r*-band light-weighted birth ISM pressure and stellar age in the upper and lower panels, respectively, within logarithmically binned 2D projected concentric elliptical shells with semimajor axis r/r_e (note that we use the locations of the stars at $z = 0.1$, not at their formation time). Thick lines show values averaged over all galaxies, while filled regions show 10−90th percentiles. The average birth pressure profiles are not very different between the three simulations, except with more scatter in HiM-50 than in LoM-50 or Ref-50. The age profiles for Ref-50 and LoM-50 are similar, but stars in HiM-50 galaxies are younger by $\approx 1-2$ Gyr for $r < r_e$.

important test of the HiM-50 model to establish whether observations that are sensitive to the high-mass end of the IMF find its slope becomes shallower toward the centres of high-mass galaxies.

These strong radial IMF gradients are a consequence of similar gradients in birth ISM pressure, which we show explicitly in the upper panel of Fig. 6 for our Sigma150 galaxies.[3] For all of our simulations, including Ref-50, birth ISM pressure increases by over 2 orders of magnitude from the outskirts to the centre. Interestingly, HiM-50 exhibits much more scatter in the central $r < 0.3\,r_e$ than in either the Ref-50 or LoM-50 simulations, which translates into the greater scatter in the IMF slope in HiM-50 than in LoM-50 (relative to the range over which it is varied in each case), shown in Fig. 5. This greater diversity in birth ISM pressures is likely a consequence of the fact that stellar feedback is burstier in HiM-50 due to the shallower high-mass slope of the IMF in high-pressure

---

[3]Note that the profiles presented in Fig. 6 use the locations of the stars at $z = 0.1$, rather than at their formation, and thus may be subject to radial migration (e.g. fig. 9 of Furlong et al. 2017). However, since radial migration affects all other $z = 0.1$ radial profiles presented in this work in the same way, showing these pressure and age profiles at $z = 0.1$ allows us to interpret our IMF trends.

environments, potentially leading to a less uniform ISM and thus a broader range of ISM pressures.

3.2.2 Mass-to-light excess radial gradients

Many observational IMF studies parametrize the IMF via the excess M/L ratio relative to that expected given a fixed reference IMF. We refer to this quantity as the M/L excess, or MLE. The MLE is directly related to what dynamical IMF studies actually measure, and is easily computed given a best-fitting IMF in spectroscopic studies. We define the MLE in the r band as

$$\mathrm{MLE}_{r,\mathrm{Kroupa}} = \frac{(M/L_r)}{(M/L_r)_{\mathrm{Kroupa}}}. \tag{1}$$

Note that here we use a non-logarithmic definition and compare M/L relative to a Kroupa IMF (in contrast to the logarithmic, Salpeter-relative definition used in Papers I and II) to facilitate comparison with observational studies that tend to use the same definition.

In the upper panel of Fig. 7, we plot $\mathrm{MLE}_{r,\mathrm{Kroupa}}$ measured within 2D projected elliptical concentric shells as a function of r/r_e for our Sigma150 galaxies at $z = 0.1$. For both simulations, the MLE is consistent with a Kroupa IMF at large radii (greater than a few r_e), gradually transitioning to larger values toward the centre. For LoM-50, all galaxies show clear negative radial gradients, while HiM-50 galaxies show much greater diversity: some have negative MLE gradients as strong as those in LoM-50, while others show no gradient at all. This diversity occurs despite the strong radial gradients in the IMF high-mass slope for the HiM-50 simulation, and is likely due to the additional dependence of the MLE on age when the high-mass slope is shallower than that for the reference IMF (Papers I and II). The lower panel of Fig. 6 shows that the mean r-band light-weighted age exhibits strong variation within r_e of the Sigma150 galaxies in HiM-50, leading to the diversity in MLE. For both simulations, these radial trends in the MLE explain the aperture effects in the MLE–σ_e relation we saw in Paper I.

We compare our radial MLE trends with those for various observed galaxies in the upper panel of Fig. 7. As a yellow line, we show the radial MLE gradient of M87 derived spectroscopically by Sarzi et al. (2018), where we have performed a by-eye fit through their data points, assigning it 0.2 dex scatter. Oldham & Auger (2018a) also obtain a negative gradient when inferring the spatially resolved MLE in M87 dynamically (yellow points), which is offset systematically to lower MLE values by about 0.2 dex relative to the Sarzi et al. (2018) result. We also compare with spectroscopic results for XSG1 (pink points; La Barbera et al. 2016), NGC 1399 (grey points; Vaughan et al. 2018b), NGC 4552 (purple points; Martín-Navarro et al. 2015b), and NGC 1277 (black points; Martín-Navarro et al. 2015d). For the latter two studies, we convert Γ_b to $\mathrm{MLE}_{r,\mathrm{Kroupa}}$ assuming their published age gradients. Finally, as a cyan line, we show the radial MLE trend of van Dokkum et al. (2017), which is a fit to the spectroscopically determined MLE as a function of radius for six massive ETGs with $\sigma \sim 200 - 340\,\mathrm{km\,s^{-1}}$.

For most of these observed systems, the MLE varies from super-Salpeter in the centre to Chabrier-like at around $0.4\,r_e$, while NGC 1399 and NGC 1277 remain Salpeter-like out to at least $\approx 1\,r_e$. Our simulated galaxies make qualitatively the same transition, but at larger radii, near or slightly above $1\,r_e$. Given the wide diversity in the observed trends, it is difficult to rule out either IMF parametrization with this test. Indeed, LoM-50 galaxies rise to larger values of MLE than HiM-50, which may be more consistent with most of these observed trends at the smallest radii. On the other hand, HiM-50 is more consistent with the Kroupa-like MLE values in some of
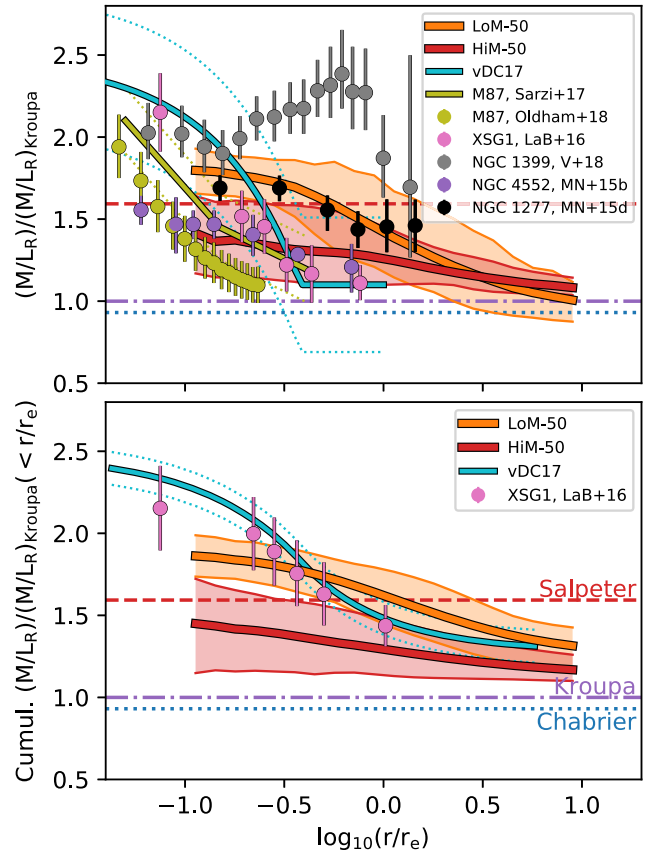
Figure 7. Radial variations in the r-band mass-to-light excess relative to a Kroupa IMF, $\mathrm{MLE}_{r,\mathrm{Kroupa}}$, within ETGs with $\sigma_e > 150\,\mathrm{km\,s^{-1}}$ in the LoM-50 (orange) and HiM-50 (red) simulations at $z = 0.1$. Radii are normalized to their r-band half-light radii, r_e. Solid thick lines show mean values averaged over all galaxies in each r/r_e bin, while solid filled regions show 10–90th percentiles. In the upper panel, we show $\mathrm{MLE}_{r,\mathrm{Kroupa}}$ measured within logarithmically binned 2D projected concentric elliptical shells with semimajor axis r/r_e, while the lower panel shows mean luminosity-weighted $\mathrm{MLE}_{r,\mathrm{Kroupa}}$ within circular 2D projected apertures of radius r/r_e. Radial MLE gradients for various observed ETGs are overplotted (see the legend and text). Horizontal red dashed, purple dotted–dashed, and blue dotted lines mark the expected values for universal Salpeter, Kroupa, and Chabrier IMFs, respectively. For both LoM-50 and HiM-50, the IMF is heavy in the centres and transitions to Kroupa-like at a few times r_e, qualitatively consistent with observations (although note that HiM-50 agrees with the spectroscopic observational studies for the wrong reasons; see Fig. 8).

the observations at $r/r_e \approx 1/3$–1, and with the shallow MLE gradient in NGC 4552 at all radii. The MLE values inferred for NGC 1399 are much larger than those for the other observed and simulated ETGs; the reason for this is unclear, but Vaughan et al. (2018b) speculate that these variances could be due to either differences in SPS modelling or the stochastic nature of galaxy formation. We thus conclude that both LoM-50 and HiM-50 are consistent with the overall observed radial MLE gradients (although in Section 3.2.3, we show that HiM-50 agrees with the MLE gradients derived from these spectroscopic studies for the wrong reasons). We reiterate that these radial variations were not considered in the calibration of our IMF variation prescriptions.

Also of interest is the cumulative MLE measured within circular apertures of increasing radius, which we plot in the lower panel of Fig. 7. Again we see negative radial gradients, but with shallower

slopes since the outer bins now contain the light from the central regions as well. We compare with spectroscopic results for six ETGs by van Dokkum et al. (2017) and for XSG1 from La Barbera et al. (2016). Both simulations agree with these observations at r_e, which is unsurprising given that they were calibrated to match the observed MLE$_r$−σ_e relation (though only using data from Cappellari et al. 2013b), where MLE$_r$ is measured within r_e. At smaller radii, the simulated gradients are shallower than the observed trends. However, LoM-50 galaxies are in excellent agreement with XSG1, and given the diversity in MLE gradients inferred from observations shown in the upper panel of Fig. 7, it is unclear if these discrepancies are robust.

Note as well that some studies find evidence for a lack of radial IMF gradients in high-mass ETGs. For example, Davis & McDermid (2017) use gas kinematics to infer the dynamical MLE radially within seven ETGs, finding that, although the IMF seems to vary between galaxies, there is no systematic radial gradient. This data would thus support the HiM-50 model, in which it is possible to have flat MLE profiles even with significant gradients in the IMF slope, owing to the age sensitivity of the relationship between MLE and high-mass IMF slope.

### 3.2.3 Dwarf fraction radial gradients

Another method of diagnosing the IMF is via the fraction of mass contributed by low-mass relative to high-mass stars. This quantity is much closer to what is actually measured when inferring the IMF from gravity-sensitive stellar absorption features, compared with the IMF slope or MLE. Since in the old stellar populations present in typical ETGs, we expect that stars with $m \gtrsim 1\,\mathrm{M}_\odot$ should have died off, we define this fraction as

$$F_{0.5,1} = \frac{\int_{0.1}^{0.5} M\,\Phi(M)\mathrm{d}M}{\int_{0.1}^{1} M\,\Phi(M)\mathrm{d}M}. \tag{2}$$

where $\Phi(M)$ is the IMF. We already showed in Paper I that this fraction, measured galaxy-wide, increases with σ_e in LoM-50 galaxies, in agreement with spectroscopic IMF studies (e.g. Conroy & van Dokkum 2012; La Barbera et al. 2013). In the upper panel of Fig. 8, we plot $F_{0.5,1}$ as a function of radius for our Sigma150 galaxies at $z = 0.1$. Consistent with the IMF slope gradients seen in Fig. 5, we find a strong negative gradient in $F_{0.5,1}$ for LoM-50, transitioning from Salpeter to Chabrier-like at around r_e. For HiM-50, the trend is much shallower because $F_{0.5,1}$ is not very sensitive to high-mass slope variations. Interestingly, HiM-50 shows a shallow but positive radial $F_{0.5,1}$ gradient due to the shallower high-mass IMF slopes in the galaxy centres (see Fig. 5).

We compare these $F_{0.5,1}$ radial profiles with results for M87 (yellow line; Sarzi et al. 2018), XSG1 (pink points; La Barbera et al. 2016), NGC 4552 (purple points; Martín-Navarro et al. 2015b), and NGC 1277 (black points; Martín-Navarro et al. 2015d), where for all of these studies we have converted the radial profiles of the high-mass IMF slope of a 'Bimodal' IMF (Γ_b) to profiles in $F_{0.5,1}$. All of these studies find negative gradients in $F_{0.5,1}$, consistent with LoM-50, although our simulated trend is shifted toward larger radii. HiM-50, on the other hand, is inconsistent with these studies, implying that a prescription that varies only the high-mass slope of the IMF towards values shallower than Salpeter is unable to explain these observations.

An alternative definition of the dwarf-to-giant ratio is the fraction of the *luminosity* that is contributed by low-mass ($m < 0.5\,\mathrm{M}_\odot$) dwarf stars, f_{dwarf}. It has been shown by Alton et al. (2017) that this
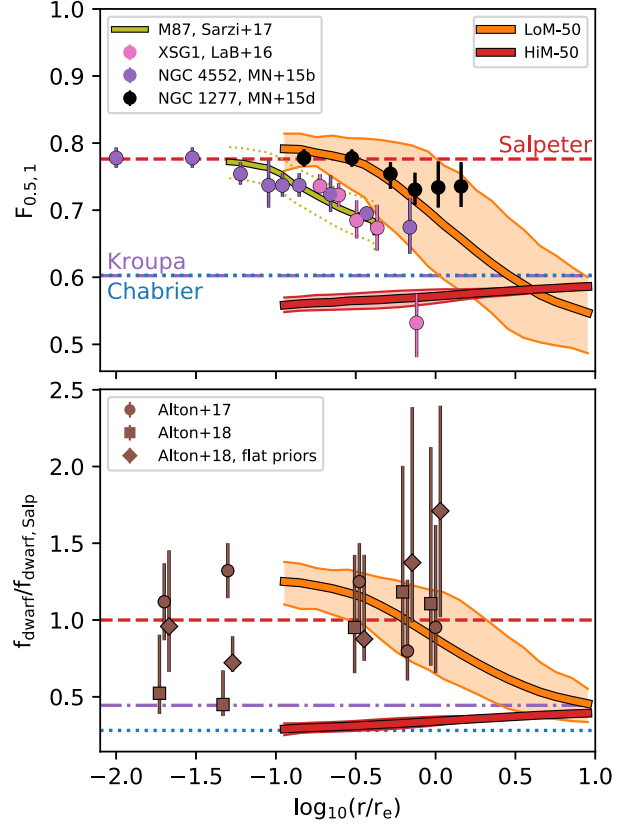
Figure 8. As Fig. 7, but now showing dwarf-to-giant ratio radial profiles. In the upper panel, we define this ratio as the mass fraction of stars with $m < 0.5\,\mathrm{M}_\odot$ relative to those with $m < 1\,\mathrm{M}_\odot$ in the IMF, $F_{0.5,1}$. In the lower panel, this ratio is defined as the fraction of the total r-band luminosity contributed by low-mass ($m < 0.5\,\mathrm{M}_\odot$) stars at $z = 0.1$, f_{dwarf}. Due to the dependence of this quantity on the age of the stellar population, in each bin we divide by the value computed for a fixed Salpeter IMF, given the same ages and metallicities of the stars. Both quantities are measured within logarithmically binned 2D concentric elliptical shells of semimajor axis r/r_e. In the upper panel, we compare with $F_{0.5,1}$ profiles found for M87 (yellow line), XSG1 (pink points), NGC 4552 (purple points), and NGC 1277 (black points). In the lower panel, we show the average f_{dwarf} for stacked spectra of eight ETGs from Alton et al. (2018) as brown squares with error bars. Brown diamonds show their results assuming a flat prior in f_{dwarf}, while brown circles show their results for the same galaxies using older SPS models and fewer absorption features (Alton et al. 2017). Horizontal red dashed, purple dotted–dashed, and blue dotted lines mark the expected values for universal Salpeter, Kroupa, and Chabrier IMFs. While LoM-50 galaxies match the observed dwarf-to-giant ratio radial gradients, the near-constant Kroupa/Chabrier values for HiM-50 galaxies are in tension with the observations.

quantity correlates very strongly with the EWs of IMF-sensitive stellar absorption features, and thus may be a better diagnostic of the low-mass regime of the IMF than $F_{0.5,1}$. However, since f_{dwarf} by itself is also dependent on age, we normalize f_{dwarf} for our galaxies by $f_{\mathrm{dwarf,\,Salp}}$, the value that would have been obtained had the stars evolved instead with a Salpeter IMF, given the same ages and metallicities. Our (r-band-weighted) $f_{\mathrm{dwarf}}/f_{\mathrm{dwarf,\,Salp}}$ radial profiles are presented in the lower panel of Fig. 8, where we find qualitatively the same gradients as in the case of $F_{0.5,1}$.

Alton et al. (2018) spectroscopically measure the radially resolved IMF in stacked spectra of seven ETGs, where they parametrize the IMF by f_{dwarf}. We show their main results as brown

squares in Fig. 8. They do not provide $f_{\text{dwarf, Salp}}$ for these stacks, so we have normalized their results by the $f_{\text{dwarf, Salp}}$ at an age of 10 Gyr presented in table C2 of Alton et al. (2017), multiplied by the ratio age/(10 Gyr). This procedure assumes a linear relationship between $f_{\text{dwarf, Salp}}$ and age, which is the case for our variable IMF simulations. The error bars include the uncertainty in the age.

Owing to the large scatter of the Alton et al. (2018) results, they are consistent with both a flat IMF gradient and the steep negative f_{dwarf} gradient in LoM-50 galaxies. This apparent paradox is also due in part to the fact that for LoM-50, f_{dwarf} transitions to a Kroupa value at around r_e, which is where the observations stop due to limited S/N. Deeper observations toward the outskirts of these galaxies would be required to establish if their IMF gradients are truly flat.

Note as well that Alton et al. (2018) find that f_{dwarf} is sensitive to assumptions made in the modelling of these galaxies. To demonstrate this sensitivity, as grey points we show the results of Alton et al. (2018) where they impose flat priors on f_{dwarf} itself (rather than on the low-mass IMF slopes; brown diamonds). This procedure increases the $f_{\text{dwarf}}/f_{\text{dwarf, Salp}}$ values in the central regions. For completeness, we also include the results of Alton et al. (2017) as brown circles, where the same analysis was performed on the same galaxies, except with fewer absorption features and a less up-to-date SPS model. Here, f_{dwarf} becomes super-Salpeter at small radii. Thus, spectroscopic inferences of the IMF are quite sensitive to the methods used (even on the same galaxies), leading to potentially strong systematic errors. A better understanding of the systematics involved in spectroscopic modelling, as well as higher resolution in simulations, will be required to quantitatively compare the IMF in the inner regions of simulated and observed galaxies.

Overall, we find that radial IMF gradients are a natural prediction of models in which the IMF is a function of local physical conditions in the ISM (in our case the pressure at which the stellar populations are born). For low-mass slope variations, our radial gradients in the IMF low-mass slope, MLE, and dwarf-to-giant ratio are all in agreement with observational IMF studies which find such gradients, but this model may not be able to explain studies that do not find such gradients. HiM-50, on the other hand, is perhaps more consistent with the diversity in the MLE radial gradients from observational studies which can range from strongly negative to flat, but is inconsistent with the negative radial dwarf-to-giant ratio gradients inferred from spectroscopic studies. Stronger consensus from observational studies will be pivotal in further constraining proposed IMF variation prescriptions.

3.3 Radial gradients in stellar population properties

Since the IMF varies strongly with radius, it is also interesting to investigate how the gradients of other stellar properties are affected by variations in the IMF. Here, we investigate gradients in metallicity, [Mg/Fe], and r-band M/L ratio for each galaxy binned radially in the same logarithmically spaced elliptical bins as in the previous section. We plot these results in Fig. 9 for our Sigma150 samples in Ref-50, LoM-50, and HiM-50 at $z = 0.1$.

The upper panel of Fig. 9 shows the radial metallicity profiles of our simulated galaxies, all of which have strongly negative gradients. Since, as we saw in Paper I, LoM-50 galaxies showed the same stellar mass–metallicity relation as Ref-50, it is unsurprising that they also have similar metallicity gradients. While HiM-50 galaxies exhibit the same gradient, the profiles are normalized to larger metallicity by ≈ 0.2 dex at all radii. This is the result of a higher production of metals due to a top-heavy IMF. Indeed, the offset appears to be strongest at small radii, where the IMF is most top
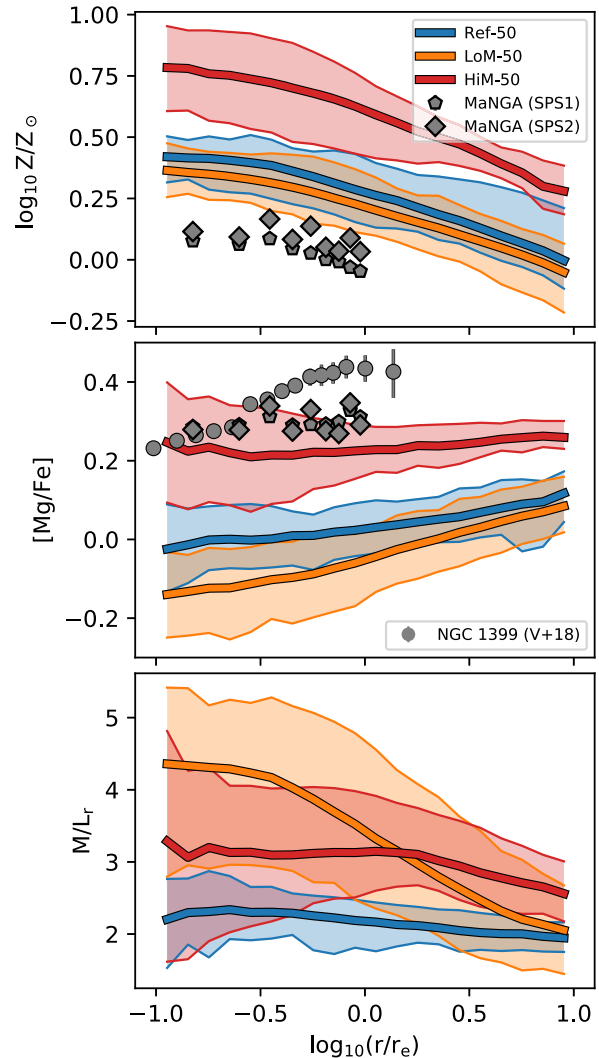
Figure 9. As Fig. 6 but showing, from top to bottom, radial gradients in the stellar metallicity, stellar α-enhancement [Mg/Fe], and r-band stellar M/L ratio for our Sigma150 ETGs. We show metallicity and [Mg/Fe] gradients for high-mass galaxies from SDSS-IV–MaNGA from Parikh et al. (2018), where pentagons and diamonds correspond to using two different SPS models. The [Mg/Fe] radial gradient in NGC 1399 is shown as grey circles (Vaughan et al. 2018b). While negative metallicity gradients are preserved in all of our simulations, the [Mg/Fe] gradients are more positive and nearly flat for LoM-50 and HiM-50, respectively. M/L gradients are negative in LoM-50, while in HiM-50 the gradients are much more diverse within r_e.

heavy in HiM-50. For comparison we show the metallicity gradients in high-mass ETGs found with SDSS-IV–MaNGA by Parikh et al. (2018, symbols as in Fig. 5). The shapes of the simulated profiles agree well with the observed results, but with some systematic offsets in normalization. However, these offsets are consistent with the factor two uncertainty in the nucleosynthetic yields in the simulations (Wiersma et al. 2009b) as well as the systematic offsets between different metallicity calibrators which can be as high as 0.7 dex (Kewley & Ellison 2008), and are thus not particularly constraining.

In the middle panel of Fig. 9, we show radial [Mg/Fe] profiles for our simulated ETGs. The profile of Ref-50 is fairly flat out to $1\, r_e$, and slowly rises beyond it. That of HiM-50 is even flatter but, as for the metallicity gradients, it is offset by ≈ 0.2–0.3 dex. LoM-50,

however, shows steeper positive radial gradients due to a deficit of α-elements in the inner regions. These results are in broad agreement with [Mg/Fe] gradients in observed galaxies which seem to vary on a case-by-case basis from either being flat (Mehlert et al. 2003; Parikh et al. 2018), to weakly positive (Spolaor et al. 2008; Brough et al. 2007), or strongly positive (as is the case for NGC 1399; Vaughan et al. 2018b). The offsets between our simulations relative to Ref-50 are consistent with those for the (galaxy-wide) [Mg/Fe]$-\sigma_e$ relation seen in Paper I, and are due to the decreased (increased) number of type II SNe resulting from a steeper (shallower) IMF slope in LoM-50 (HiM-50).

The *r*-band *M/L* ratio radial profiles are shown in the lower panel of Fig. 9. While in Ref-50, the gradient is generally flat with $M/L_r \approx 2$–3 $M_\odot / L_\odot$ at all radii, in LoM-50, it increases by a factor ≈ 2 toward the centre, as expected given the MLE gradients seen in Fig. 7. HiM-50 ETGs have a much greater diversity in *M/L*, ranging from 1 to 5 below $0.3\,r_e$. These non-constant *M/L* ratios may have important consequences for dynamical mass measurements (see Bernardi et al. 2018; Sonnenfeld et al. 2018; Oldham & Auger 2018b), particularly when such masses are used to infer the IMF (Cappellari et al. 2013b). Here, we have shown that in the case of IMF variations, the assumption of a constant *M/L* within r_e is not justified.

3.4 IMF versus local quantities

We now study the correlation between the IMF (parametrized by the MLE), and local galaxy properties. To this end, we investigate the trends between MLE and metallicity, [Mg/Fe], and age, measured in the same logarithmically spaced elliptical annuli as in the previous subsections. Crucially, the question of whether or not such correlations exist can depend on how the data are combined. First we ask, if we consider the data from all of the radial bins in all of the Sigma150 galaxies simultaneously, is there a correlation between MLE and local properties? This procedure is similar to what is done by some observational studies such as Martín-Navarro et al. (2015c) or van Dokkum et al. (2017).

In the top left panel of Fig. 10, we show MLE$_{r,Kroupa}$ as a function of stellar metallicity. Here, each thin line shows the trend for an individual galaxy in radial bins, while thick solid lines show the best least absolute deviation (LAD) fit result when fitting to all galaxies simultaneously, with corresponding Spearman *r*-values and their *p*-values indicated in the upper left of each panel for LoM-50 (orange) and HiM-50 (red). For both simulations, we see overall a significant positive relation, likely due to the fact that both the IMF and metallicity vary radially monotonically. For comparison, we show the same trend for the six ETGs studied by van Dokkum et al. (2017) as a thick cyan line,[4] as well as the relation by Martín-Navarro et al. (2015c), and that for the highest mass bin ($10.5 < \log_{10} M_\star / M_\odot < 10.8$) of SDSS–MaNGA by Parikh et al. (2018). All of these studies find strong positive correlations of the IMF slope with increasing local metallicity, in good agreement with our findings. However, the shallower slope of this relation for HiM-50 galaxies is in slight tension with the observations. Note that our IMF (and MLE) does not depend physically on metallicity. Thus, a strong, tight correlation with metallicity can be expected even if the IMF varies with another property of the ISM, in our case pressure.

---

[4]We have shifted the van Dokkum et al. (2017) values to the right by 0.3 dex to convert from [Fe/H] to $Z/Z_\odot$, given their fairly consistent [Mg/Fe] values of 0.3 dex and the relation from Thomas, Maraston & Bender (2003).

The above analysis may be sensitive to correlations between the MLE and global galaxy properties if the range of global values among galaxies is larger than the range of local values within them. To eliminate such effects, we also measure the slope of this correlation for each individual galaxy. We show these results in the upper right panel of Fig. 10. For nearly every Sigma150 ETG in both LoM-50 and HiM-50, we find a significant positive correlation between the local MLE and local metallicity. We compare with the slopes of the observed relations shown in the left-hand panel. For Parikh et al. (2018), we manually perform a least-squares fit to their data only for the highest mass bin, rather than over all three mass bins as in that paper, as the latter analysis would be sensitive to a global correlation between MLE and age (as can be seen by the lack of overlap in radially resolved age in their highest and lowest mass galaxy bins in their fig. 17). The slopes of our relations for individual galaxies in LoM-50 are consistent with those observed, while the slopes for HiM-50 galaxies, albeit consistently positive, are shallower than the observed trends. Note as well that, strictly speaking, it is not completely fair to compare HiM-50 with these observational studies since they measure the IMF spectroscopically, constraining the dwarf-to-giant ratio. Indeed, the dwarf-to-giant ratio in HiM-50, being relatively constant with radius (Fig. 8) would not correlate with changes in local stellar properties. We also do not see any correlation of these best-fitting slopes with σ_e for these high-σ_e galaxies.

We also perform the same investigation into the correlation between local MLE$_{r,Kroupa}$ and local [Mg/Fe], shown in the middle row of Fig. 10. Here, we see strikingly different behaviour. When taking all of the galaxies together (solid thick lines in the middle left panel), we find a strong negative correlation of MLE$_{r,Kroupa}$ with [Mg/Fe] in LoM-50, while that for HiM-50 galaxies is positive. This difference between the simulations opens up a novel method of discriminating between these IMF parametrizations. When looking at galaxies individually, this negative relation persists for the majority of LoM-50 galaxies, but no systematic trend is obvious for our five HiM-50 ETGs. Thus, the positive relation seen when combining results from these five HiM-50 galaxies likely reflects the strong global MLE–[Mg/Fe] relation for HiM-50 ETGs (see fig. 2 of Paper II). Care should thus be taken when inferring local IMF relations to first remove global trends between galaxies.

These correlations between the MLE and [Mg/Fe] may be in tension with radially resolved IMF studies, in which typically no significant correlation between the IMF and local [Mg/Fe] is found (e.g. Martín-Navarro et al. 2015c; van Dokkum et al. 2017; Parikh et al. 2018, but see Sarzi et al. 2018). However, the best-fitting slopes from Parikh et al. (2018), while consistent with zero, are also consistent with our findings, both for LoM-50 and HiM-50 (middle right panel). Thus, the correlations between the local MLE and local [Mg/Fe] may be washed out in some current studies by observational uncertainties.

In the lower row of Fig. 10, we perform the same analysis but for the correlation between local MLE$_{r,Kroupa}$ and local stellar age. For LoM-50, when considering the entire sample together, we find a weak positive correlation with age (shown by the solid orange line and corresponding Spearman *r*-value in the lower left panel). However, the same is not true for individual galaxies (orange points in the lower right panel), where the best-fitting slope tends to scatter around 0 at all σ_e. For HiM-50, we do not find any systematic correlation with local age in either case. Thus, for both simulations, we see no significant systematic correlation between MLE and age within individual galaxies. Indeed, the positive trend for LoM-50 seen in the lower left panel merely reflect the strong dependence
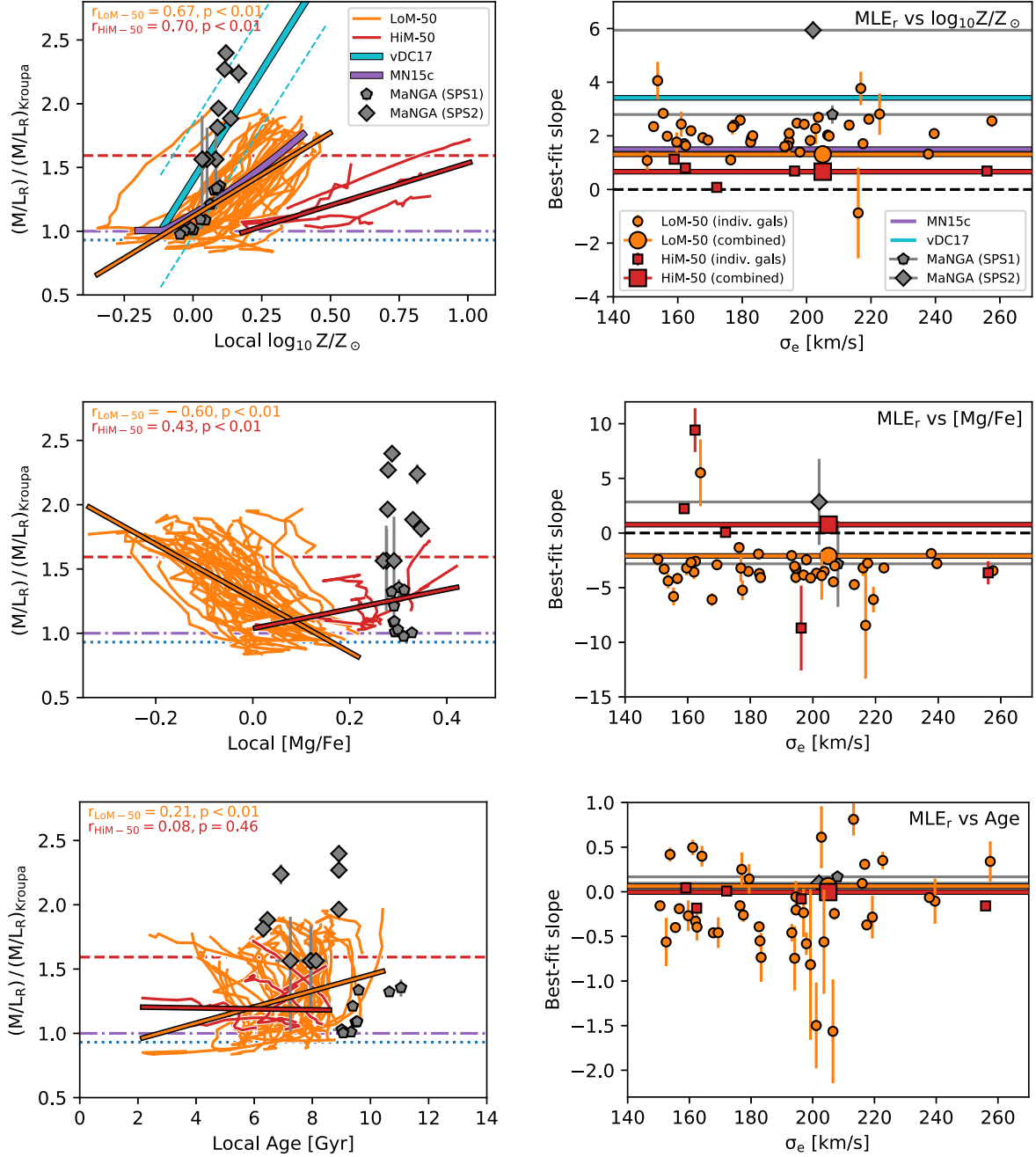
Figure 10. Left-hand column: local excess *r*-band *M/L* relative to a Kroupa IMF (MLE$_{r,Kroupa}$) as a function of local stellar metallicity (upper row), stellar [Mg/Fe] (middle row), and stellar age (lower row) within ETGs with $\sigma_e > 150$ km s^{-1} from LoM-50 (orange) and HiM-50 (red) at $z = 0.1$. All quantities are *r*-band light-weighted. Each thin coloured line shows values for an individual galaxy in logarithmically spaced radial bins from 1 kpc to 10 r_e. LAD fits to all galaxies simultaneously are shown thicker, outlined in black, with Spearman *r*-values and their *p*-values indicated in each panel. Trends for high-mass ETGs from SDSS-IV–MaNGA for two different SPS models from Parikh et al. (2018) are shown as grey pentagons and diamonds, respectively. The observed local MLE–metallicity relation found by Martín-Navarro et al. (2015c) is shown as a purple solid line and that for six massive ETGs from van Dokkum et al. (2017) is shown as a solid cyan line with intrinsic scatter shown as cyan dashed lines. Expected MLE values for fixed Salpeter, Kroupa, and Chabrier IMFs are indicated with horizontal red dashed, purple dotted–dashed, and blue dotted lines, respectively. Right-hand column: logarithmic slopes of LAD fits to the local MLE$_{r,Kroupa}$ as a function of local properties within individual galaxies with $\sigma_e > 150$ km s^{-1} in LoM-50 (orange circles) and HiM-50 (red squares), plotted as a function of σ_e. Each small point in the right-hand column corresponds to a thin line in the left, while larger symbols show the slopes of the LAD fits to all of these galaxies simultaneously. MLE$_{r,Kroupa}$ systematically correlates positively with local metallicity in both simulations, in qualitative agreement with the observations. The correlation with local [Mg/Fe] is negative and positive in LoM-50 and HiM-50, respectively, but for HiM-50, it differs substantially between galaxies. When combining results from all galaxies, MLE$_{r,Kroupa}$ increases weakly with local age for LoM-50, but on average decreases for individual galaxies. No correlation with local age is found for HiM-50 galaxies.

of the MLE on age when measured 'galaxy-wide' (see fig. 2 of
Paper II). These differences are subtle, but are extremely important
in trends between the IMF and local properties in observational
studies, especially when combining results from galaxies with a
wide range of global properties, as is often necessary to obtain
sufficiently high S/N ratio out to large radii.

Overall, these results highlight the importance of removing global
trends between the MLE and integrated galaxy properties before
interpreting trends within galaxies. For both simulations, we find
strong positive correlations of MLE with local metallicity, and the
average negative (for LoM-50) and positive (for HiM-50) correla-
tions with [Mg/Fe] will be useful in discriminating between scenar-
ios in which the IMF becomes either bottom heavy or top heavy in
high-pressure environments.

4 REDSHIFT DEPENDENCE OF GALAXY PROPERTIES

In Paper I, we investigated the galaxy-wide correlations between
IMF-related diagnostics such as the MLE, $F_{0.5,1}$, and ionizing flux
with global galaxy properties such as σ_e and SFR, finding good
agreement with observations. In this section, we switch from the
spatially resolved properties discussed in the previous sections to
investigate the evolution of these (global) IMF scaling relations
(Section 4.1), as well as the effect that our IMF variation models
have on the evolution of the cosmic properties in the simulations
(Section 4.2).

4.1 Redshift dependence of the IMF

Some models of IMF variation in the literature invoke time-
dependent IMF variations to explain the enhanced dwarf-to-giant
ratios as well as high metal enrichment in high-mass ETGs (e.g.
Arnaud et al. 1992; Weidner et al. 2013; Ferreras et al. 2015;
Martín-Navarro 2016, first a top-heavy starburst, then a prolonged
bottom-heavy mode). Since our IMF depends on pressure, and typi-
cal birth ISM pressures decrease with time, our average IMF is also
implicitly time-dependent. Indeed, for our HiM IMF prescription,
high-pressure starbursts will naturally be given a top-heavy IMF
while lower pressure, less rapid star formation will proceed with an
IMF closer to Kroupa (bottom heavy).

We now investigate the evolution of IMF-related diagnostics
in our simulations for unresolved, galaxy-averaged properties. As
in Papers I and II, we compute these properties as r-band light-
weighted mean quantities measured within a circular projected
aperture of radius r_e. Also for consistency with Papers I and II,
we redefine the MLE as

$$\mathrm{MLE}_{r,\mathrm{Salp}} = \log_{10}(M/L_r) - \log_{10}(M/L_r)_{\mathrm{Salp}}, \tag{3}$$

which is effectively a rescaled version of $\mathrm{MLE}_{r,\mathrm{Kroupa}}$.

In Fig. 11, we show the median relation between $\mathrm{MLE}_{r,\mathrm{Salp}}$ and
σ_e at $z = 0.1, 1, 2,$ and 4 (different line styles) for LoM-50 (orange)
and HiM-50 (red) for all galaxies with $\sigma_e > 10^{1.6}$ km s^{-1} at each
redshift. Despite being calibrated to roughly the same value at $z =$
0.1, the redshift evolution of the $\mathrm{MLE}_{r,\mathrm{Salp}} - \sigma_e$ relation differs
greatly between the two IMF prescriptions. While the MLE of
high-σ_e galaxies increases with redshift for LoM-50 galaxies, it
decreases for HiM-50 galaxies. At $z = 2$, for example, the typical
$\mathrm{MLE}_{r,\mathrm{Salp}}$ in LoM-50 is ≈ 0.1 dex higher than the $z = 0.1$ relation,
with most galaxies in this mass range having a super-Salpeter IMF.
On the other hand, galaxies in HiM-50 are ≈ 0.1 dex *lower* at $z = 2$
than at $z = 0.1$.
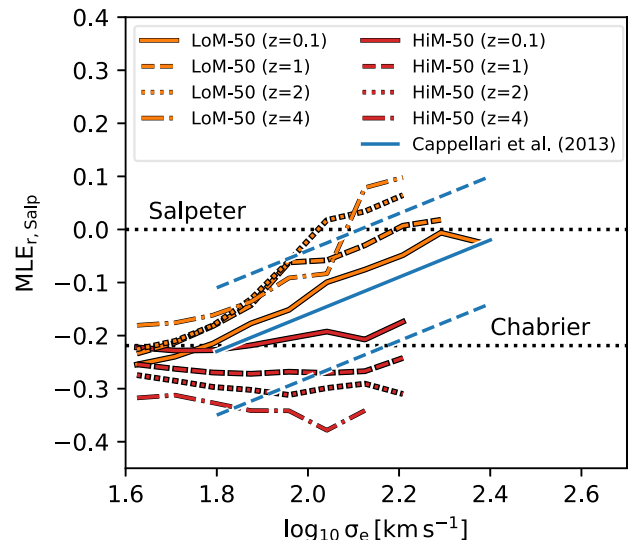
Figure 11. Galaxy-wide $\mathrm{MLE}_{r,\mathrm{Salp}}$ as a function of σ_e for LoM-50 (orange)
and HiM-50 (red) at $z = 0.1$ (solid lines), $z = 1$ (dashed lines), $z = 2$
(dotted lines), and $z = 4$ (dashed–dotted lines) for all galaxies with $\sigma_e >$
$10^{1.6}$ km s^{-1} at each redshift. Thick lines shown medians for bins with more
than five galaxies. All quantities are r-band light-weighted and measured
within the 2D projected r-band half-light radius of each galaxy. A blue solid
line indicates the Cappellari et al. (2013b) relation at $z \approx 0$, with dashed
blue lines denoting intrinsic scatter. Horizontal black dotted lines mark the
Salpeter and Chabrier $\mathrm{MLE}_{r,\mathrm{Salp}}$ values. For the LoM-50 (HiM-50) run,
galaxies have a heavier (lighter) $\mathrm{MLE}_{r,\mathrm{Salp}}$ with increasing redshift.

We can understand these differences via Fig. 12, where we show
$\mathrm{MLE}_{r,\mathrm{Salp}}$ as a function of stellar birth ISM pressure at $z = 2$ and
0.1, respectively, for stars within the half-light radius of galaxies
with $\sigma_e > 100$ km s^{-1}. Blue histograms show the distribution of
birth ISM pressures for these stars. For the LoM-50 simulation
shown in the left-hand column, we see that the $\mathrm{MLE}_{r,\mathrm{Salp}}$−pressure
relation is nearly identical at high and low redshift, due to the age
independence of the MLE for this form of the IMF (see Fig. 5
of Paper I). However, the blue histograms show that birth ISM
pressures of stars were typically much higher at $z = 2$ than at $z =$
0.1. This result is due to the fact that densities are in general higher
at higher redshift, and thus the pressures at which stars form are
also higher.

On the other hand, for the HiM-50 simulation, not only were the
stars formed at higher pressure at high redshift, but also the shape of
the $\mathrm{MLE}_{r,\mathrm{Salp}}$−pressure relation changes over time, becoming more
'heavy' as time goes on. This effect is due to the age dependence
of the MLE for an IMF with a shallow high-mass slope. Stellar
particles at high pressure are born 'light', with low MLE due to a
prevalence of high-mass stars, but over time become 'heavy' due
to stellar evolution removing these bright stars and leaving behind
stellar-mass BHs and NSs.

Martín-Navarro et al. (2015a) recently inferred from spectro-
scopic observations that the IMF of ETGs at $z \approx 1$ is consistent
with that of ETGs at low redshift. To compare with their results, we
plot in Fig. 13 the mass ratio between stars with $m < 0.5 \, M_\odot$ and
$< 1 \, M_\odot$ in the galaxy-averaged IMF, $F_{0.5,1}$ (equation 2), as a func-
tion of σ_e. As with the MLE, $F_{0.5,1}$ becomes 'heavier' (i.e. higher
$F_{0.5,1}$ values) at larger redshift for LoM-50. However, since $F_{0.5,1}$
is rather insensitive to the high-mass IMF slope, the correlation
remains flat at the Chabrier value for HiM-50 at all redshifts.
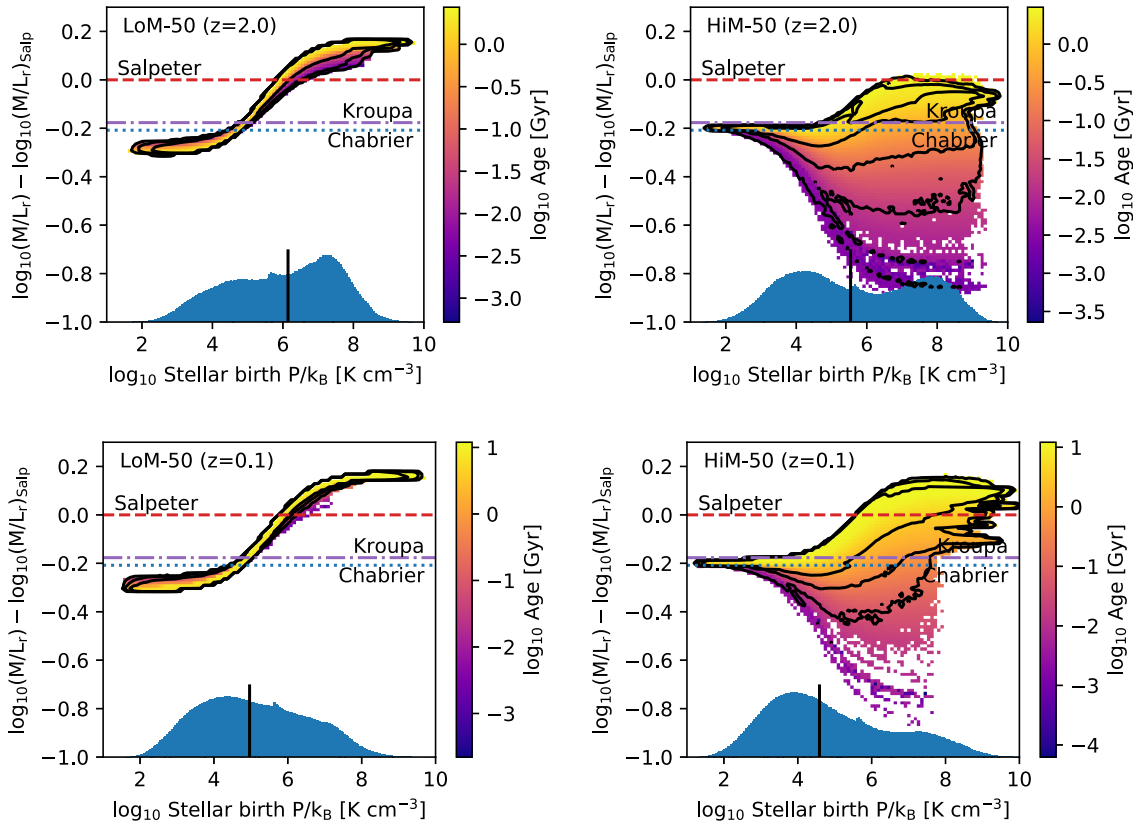
Figure 12. Redshift dependence of the MLE$_{r,\,\text{Salp}}-\sigma_e$ relation for individual stellar particles in the LoM-50 (left-hand column) and HiM-50 (right-hand column) simulations. 2D histograms in the upper and lower rows show MLE$_{r,\,\text{Salp}}$ as a function of birth ISM pressure for stars within the half-light radius of galaxies with $\sigma_e > 100\,\text{km}\,\text{s}^{-1}$ at $z = 2$ and 0.1, respectively. 2D bins are coloured by the mean age of stars within each bin. Contours show boundaries of (1000, 100, and 10) stars per bin. Blue 1D histograms show the normalized distribution of birth ISM pressures on a linear scale; and black horizontal lines show the medians of these distributions. In the LoM-50 case, higher birth ISM pressures at high z result in a larger fraction of dwarf stars than at $z = 0.1$. As MLE$_{r,\,\text{Salp}}$ is relatively independent of age for this IMF, the effect is immediate. In the HiM case, most stars born at high pressure have not lived long enough for the MLE$_{r,\,\text{Salp}}$ to become 'heavy' (i.e. for massive stars to die off, reducing the light and increasing the mass due to BHs/NSs), so they still have low *M/L* ratios relative to Salpeter at this high redshift.
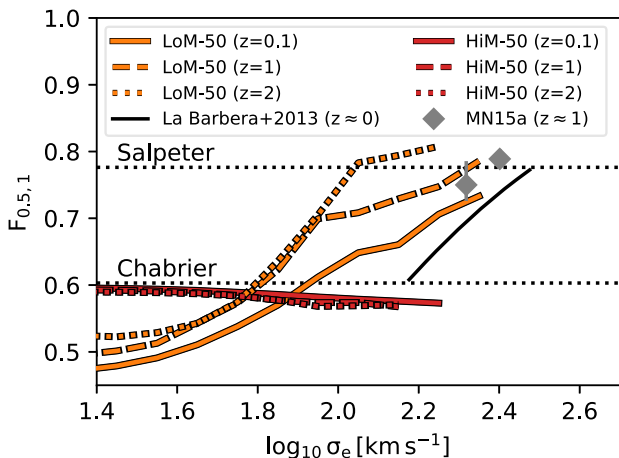
Figure 13. Redshift dependence of dwarf fractions in LoM-50 and HiM-50. The mass fraction of stars with $m < 0.5\,\text{M}_\odot$ relative to those with $m < 1\,\text{M}_\odot$ in the IMF, $F_{0.5,\,1}$, is shown as a function of σ_e. Line styles are as in Fig. 11. The result of La Barbera et al. (2013) at $z \approx 0$ (assuming a bimodal IMF) is shown as a solid black line. Values for quiescent galaxies at $z \approx 1$ from Martín-Navarro et al. (2015a) are shown as grey diamonds with 1σ error bars. The $F_{0.5,\,1}-\sigma_e$ relation evolves significantly for LoM-50, but not for HiM-50.

The result from Martín-Navarro et al. (2015a) is shown in Fig. 13 as grey diamonds, which agrees well with the trend for LoM-50 at $z = 1$. Indeed, the magnitude of the weak evolution seen in Martín-Navarro et al. (2015a) from $z = 0$ to 1 is reproduced well by LoM-50. This good agreement is quite interesting given the fact that Martín-Navarro et al. (2015a) model the increased dwarf fractions by steepening the high-mass slope of the IMF, rather than the low-mass slope as is done in our LoM model. This result highlights the degeneracy between the low- and high-mass slopes in setting the dwarf-to-giant ratio derived in spectroscopic IMF studies of old ETGs.

While of our two variable IMF models, only LoM-50 is able to reproduce observational IMF trends based on the dwarf-to-giant ratio, HiM-50 alone is consistent with those based on the H α flux of local star-forming galaxies (see Paper I). High-redshift observations of star-forming galaxies also find evidence for shallow high-mass IMF slopes in such systems (e.g. Nanayakkara et al. 2017; Zhang et al. 2018). In particular, Nanayakkara et al. (2017) find that the enhanced H α EWs of $z \approx 2$ galaxies could be explained with an IMF slope shallower than (under our IMF definition) -2.0. To compare with their data, we compute the ratio of ionizing flux to the SDSS r-band flux, f_{ion}/f_r, for our simulated galaxies, where f_{ion} is the flux of photons with $\lambda < 912$ Å, and is a proxy for the H α flux (Shivaei et al. 2018). Note that f_{ion} includes light from stars of all ages, while
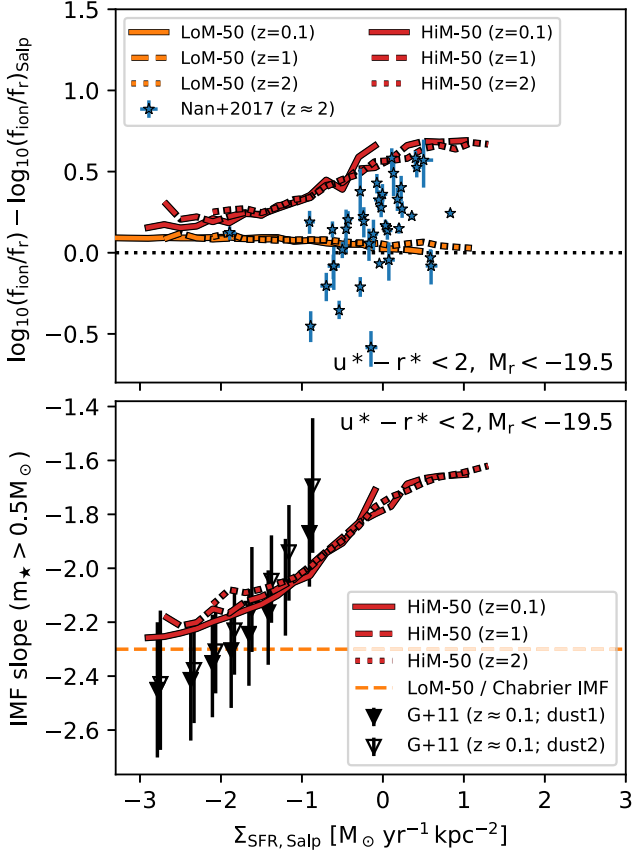
Figure 14. Upper panel: ionizing flux relative to SDSS *r*-band flux, normalized by the value expected for a Salpeter IMF, as a function of Salpeter-reinterpreted SFR surface density, $\Sigma_{SFR,Salp}$, in bright ($M_r < -19.5$), star forming (intrinsic $u^* - r^* < 2$) galaxies in LoM-50 (orange) and HiM-50 (red) at different redshifts. Line styles are as in Fig. 11. For reference, we include observations of H α EW relative to that expected for a Salpeter IMF for star-forming galaxies at $z \approx 2$ by Nanayakkara et al. (2017). Lower panel: FUV-weighted high-mass ($m > 0.5\,M_\odot$) IMF slope as a function of $\Sigma_{SFR,Salp}$ for the same galaxy sample as in the upper panel. The high-mass slope for all LoM-50 galaxies (the Chabrier value) is shown as a dashed orange line. For reference, we include observations of local star-forming galaxies by Gunawardhana et al. (2011) for two different dust extinction models. The ionizing-to-*r*-band flux ratio and IMF slopes do not evolve appreciably with redshift at fixed $\Sigma_{SFR,Salp}$ for either simulation, but for HiM-50 the relation extends to larger $\Sigma_{SFR,Salp}$, and thus larger f_{ion}/f_r and shallower high-mass IMF slopes, at higher redshift. The observed trends of shallower IMF slope or stronger H α EWs with increasing $\Sigma_{SFR,Salp}$ at all redshifts are qualitatively consistent with our HiM-50 simulation.

f_r is only computed for those with age >10 Myr. The ratio f_{ion}/f_r is then a rough proxy for H α EW, which is the H α flux relative to the continuum. To remove systematics in converting from this quantity to H α EW, we normalize by the value expected given a Salpeter IMF, making it the 'excess' f_{ion}/f_r. Since in Paper I, we found that the high-mass IMF slope correlates strongly with SFR surface density (a result of the pressure dependence of the IMF), in the upper panel of Fig. 14 we plot the excess f_{ion}/f_r as a function of Salpeter-reinterpreted SFR surface density $\Sigma_{SFR,Salp}$, at different redshifts. $\Sigma_{SFR,Salp}$ is computed as in Paper I, where $\Sigma_{SFR,Salp} = SFR_{Salp}/(2\pi r_{e,FUV}^2)$, where SFR_{Salp} is the total SFR within a 3D aperture of radius 30 pkpc multiplied by the ratio between the *GALEX* FUV flux and that expected given a Salpeter IMF, and

$r_{e,FUV}$ is the half-light radius in the FUV band. Here, we show only star-forming galaxies (intrinsic $u^* - r^* < 2$) with $M_r < -19.5$, for consistency with the selection of Gunawardhana et al. (2011).

In the upper panel of Fig. 14, we see that the excess $f_{ion}/f_r - \Sigma_{SFR,Salp}$ relation is positive for star-forming galaxies in HiM-50 but flat for those in LoM-50. It also does not evolve with redshift, but is instead extended to larger $\Sigma_{SFR,Salp}$, and thus to larger excess f_{ion}/f_r. We compare with results from the ZFIRE survey by Nanayakkara et al. (2017), shown as blue stars. We use their SFRs derived from the H α luminosity, which, due to its sensitivity to SFR on very short time-scales, is most consistent with our simulated instantaneous SFRs. For their galaxies, we compute $\Sigma_{SFR,Salp}$ as $SFR/(2q\pi r_e^2)$, where r_e is obtained by cross-matching the FourStar Galaxy Evolution Survey (ZFOURGE) galaxies with the Cosmic Assembly Near-infrared Deep Extragalactic Legacy Survey (CAN-DELS) and using sizes from Van Der Wel et al. (2012), and $q = b/a$ is the minor-to-major axis ratio. While they find a trend of increasing excess H α EW with increasing $\Sigma_{SFR,Salp}$ (in qualitative agreement with HiM-50 albeit with large scatter), their values tend to be lower than those of HiM-50, suggesting that our IMF variations may be too strong in the HiM model.

It is also interesting that the ionizing excess falls below the Salpeter value for some ZFIRE galaxies with $\Sigma_{SFR} < 1\,M_\odot\,yr^{-1}\,kpc^{-2}$. It is tempting to infer from this result that IMF high-mass slopes steeper than Salpeter are required at lower pressures. However, such low values may also result in the case that these galaxies are post-starburst systems. In this case, the long-lived stars created in the starburst event serve to enhance the continuum more than the H α flux, leading to lower H α EWs than expected for a constant star formation history, even with a fixed IMF (see fig. 17 of Nanayakkara et al. 2017). Thus, stronger constraints on their star formation histories would be required to make inferences on the IMF slope in this regime.

To aid comparison with observations of high-redshift star-forming galaxies, we show in the lower panel of Fig. 14, the high-mass slope of the IMF as a function of $\Sigma_{SFR,Salp}$ at different redshifts. For reference, we also show the IMF slope at $z \approx 0.1$ for star-forming galaxies from the Galaxy And Mass Assembly (GAMA) survey inferred by Gunawardhana et al. (2011) assuming either Calzetti (2001)/Cardelli, Clayton & Mathis (1989) or Fischera & Dopita (2005) dust corrections (dust1 and dust2, respectively). As for the ionizing fluxes, this relation does not evolve with redshift for the simulated galaxies, but shifts to higher $\Sigma_{SFR,Salp}$, making the average high-mass slope shallower in high-z star-forming galaxies. These slopes are shallower than those found for the $z \approx 2$ observations by Nanayakkara et al. (2017), for which high-mass IMF slopes of ≈ -2 may be needed to explain their H α EWs. Zhang et al. (2018) recently concluded that high-mass IMF slopes as shallow as -2.1 would be required to explain the $^{13}CO/C^{18}O$ ratios observed in $z \approx 2-3$ submillimetre galaxies, which is also steeper than predicted by HiM-50. These findings suggest that the high-mass slope may be too shallow in our HiM-50 simulation.

4.2 Redshift-dependent cosmic properties

We now briefly investigate the redshift evolution of star formation in the simulations. The upper panel of Fig. 15 shows the evolution of the cosmic comoving stellar mass density, $\rho_\star$, in our variable IMF simulations compared with Ref-50. At all redshifts, $\rho_\star$ lies systematically above and below Ref-50 in LoM-50 and HiM-50, respectively. The offsets are stronger at high redshift and gradually come into closer agreement with Ref-50 with time, where from $z =$
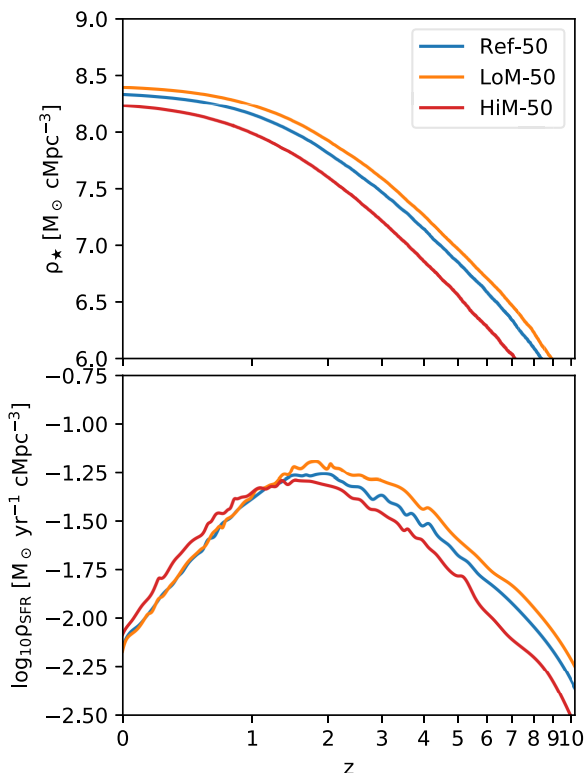
Figure 15. Comoving cosmic stellar mass density (top panel) and SFR density (bottom panel) as a function of redshift in the Ref-50 (blue), LoM-50 (orange), and HiM-50 (red) simulations. Star formation is enhanced and suppressed at high z in LoM-50 and HiM-50, respectively.

5 to 0 the offset for LoM-50 drops from $\approx$0.1 to 0.07 dex, and that for HiM-50 drops from -0.3 to -0.1 dex. The stronger offsets at high redshift are likely due to the fact that the stars that formed at the highest pressures tend to have formed earlier, while those with more Chabrier-like IMFs typically formed later. Note as well that here we plot the stellar masses directly from the EAGLE simulation, with no post-processing with FSPS. Since FSPS assumes higher remnant masses for metal-rich stellar populations than the Wiersma et al. (2009b) models built into EAGLE, $\rho_\star$ shown here for HiM-50 may be lower than that that would be derived using FSPS.

These offsets can be explained with the cosmic SFR density, ρ_{SFR}, shown in the lower panel of Fig. 15. Note that here we show the true values, rather than those that would be inferred assuming a fixed IMF. For LoM-50, ρ_{SFR} is consistent with Ref-50 at low redshift, but at $z > 1.5$, it lies systematically $\approx$0.1 dex above the Ref-50 relation. This offset is likely due to the increased SFR from the star formation law renormalization that is required observationally (see Paper I), since at high redshift, most star formation occurs at high pressure, leading to bottom-heavy IMFs and thus a higher normalization of the star formation law.

For HiM-50, the opposite is true, where at high redshift, the SFR is lower than Ref-50 by $\approx$0.1 dex. This could be due to the renormalization of the star formation law as well (which is decreased at high pressure in HiM-50), and/or due to the stronger stellar feedback associated with shallow high-mass IMF slopes. Stronger feedback would be more effective at keeping gas out of galaxies, delaying its reaccretion to later times. This hypothesis is supported by the fact that ρ_{SFR} is larger by $\approx$0.1 dex at $z < 1.5$, and the fact that the cold gas fractions are larger by $\approx$0.5 dex in high-mass galaxies in HiM-50 relative to Ref-50 and HiM-50 (see fig. 12 of Paper I).

We showed in Paper I that the *K*-band luminosity functions of Ref-50, LoM-50, and HiM-50 are all consistent with observations at $z \approx 0$. We investigated the evolution of this relation for our simulations, finding no significant difference between them. However, the poor statistics at the bright end of the luminosity functions in our (50 Mpc)^3 boxes preclude a detailed comparison, since it is at the bright (high-mass) end where the IMF is expected to have the largest impact. Simulations with larger volumes would thus be required to make a proper comparison.

5 DISCUSSION

Throughout this project (Papers I, II, and this work), we have tested a model of galaxy formation and evolution that self-consistently includes local IMF variations that have been calibrated to reproduce the observed MLE$-\sigma_e$ relation of Cappellari et al. (2013a). In this section, we discuss some of the lessons learned and propose some steps for the future.

To make the simulations self-consistent, we made the stellar feedback, star formation law, and the metal yields depend on the IMF. Ensuring that each of these processes was self-consistent was vital in capturing the full effect of the IMF variations. Interestingly, this resulted in galaxy observables such as the luminosity function and BH masses to be mostly unchanged relative to a model with a fixed Chabrier IMF.

As discussed in Papers I and II, this is partially because while the change in IMF modifies the galaxies' masses through its effect on the stellar feedback, for the luminosity function this effect is largely cancelled by the modified *M/L* ratios resulting from the IMF variations. This story is, however, further complicated by the fact that in the mass regime in which the IMF varies significantly from the Chabrier form ($M_\star \gtrsim 10^{10.5}\ M_\odot$) both stellar and AGN feedback play important roles in regulating the inflow of gas onto the galaxy. In this regime, one might expect BH feedback (and thus BH growth and the $z = 0$ BH masses) to adjust to account for the modified stellar feedback resulting from IMF variations. However, we found that our modifications to make the star formation law self-consistent precluded this (likely by adjusting the gas densities near the BHs), leading to similar BH masses as in the reference model. Thus, when performing variable IMF simulations, it is very important to include both self-consistent prescriptions for stellar feedback and the star formation law to ensure that the full effect of the IMF variations is captured and a realistic population of galaxies is produced.

For other galaxy properties, such as the metallicity and alpha enhancement, we have shown that the choice of IMF parametrization is extremely important when implementing IMF variations into galaxy formation models. Indeed, even though the LoM and HiM models produced similar MLE–σ_e relations, they resulted in very different metallicities and alpha abundances because the high-mass slope is especially important in setting the feedback strength and metal enrichment of galaxies. We thus encourage observational studies that infer the IMF slope to be careful in choosing which part of the IMF they should vary. For example, La Barbera et al. (2013) use the effect on the dwarf-to-giant ratio imprinted onto the spectra of old ETGs to constrain the IMF slope at all masses (0.1–100 $M_\odot$) or only at high masses. However, we have shown that the dwarf-to-giant ratio can be increased simply by varying the IMF only at low masses, leaving any variation of the high-mass IMF unconstrained by spectroscopic measurements of (old) ETGs. Indeed, we argue that varying only the low-mass slope is much preferred over the high-mass slope due to the strong effect the latter has on metal enrichment and stellar

feedback in galaxy formation models, making the former the simplest model that explains the observations (see also Martín-Navarro 2016).

Despite the success of our variable IMF simulations in terms of reproducing observationally inferred global and radial trends, we have shown that they are unable to simultaneously reproduce the inferred dwarf-to-giant ratios in ETGs, which prefer LoM, as well as the ionizing properties of late-type galaxies, which prefer HiM. In order to match all of these observations simultaneously, a more complex model of IMF variations, such as a hybrid of the LoM and HiM models, may be required. Indeed, the shallow high-mass slope in the HiM model was required to obtain sufficiently large MLE values from stellar remnants to reproduce the $\mathrm{MLE_r}-\sigma_e$ relation of Cappellari et al. (2013b) when the low-mass slope was kept fixed. If the low-mass slope were allowed to vary in tandem with the high-mass slope, such shallow high-mass slopes would no longer be required to obtain large MLE values, as the MLE would then increase due to a combination of excess dwarf stars *as well as* excess stellar remnants. Such a model would need to become simultaneously bottom heavy and top heavy towards higher pressure environments, possibly by steepening and levelling the low- and high-mass IMF slopes, respectively. This 'butterfly' IMF model would need to be calibrated to simultaneously reproduce the MLE and dwarf-to-giant ratios of high-mass ETGs, as well as the ionizing fluxes of strongly star-forming galaxies. A similar model has already been implemented into semi-analytic models of galaxy formation with promising potential to reconcile these observations (Fontanot et al. 2018), and would thus be interesting to implement into our self-consistent hydrodynamical, cosmological simulations.

6 SUMMARY AND CONCLUSIONS

In Paper I, we presented two cosmological, hydrodynamical simulations based on the EAGLE model that self-consistently vary the IMF to become either more bottom heavy (LoM-50) or top heavy (HiM-50) locally in high-pressure environments. These IMF prescriptions were calibrated to match the observed relation between the 'galaxy-wide' MLE relative to a fixed IMF (the MLE) as a function of stellar velocity dispersion, by respectively increasing the mass fraction of dwarfs or stellar remnants in high-pressure environments (Fig. 1). In Paper II, we showed how the MLE varies globally between galaxies as a function of various galaxy properties, including metal enrichment, age, and BH mass. In this paper, we investigate radial trends within the galaxies in these simulations to compare with the EAGLE simulations with a universal, Chabrier IMF (Ref-50) and with observed radial gradients of IMF diagnostics and abundances in high-mass galaxies, in addition to investigating the redshift dependence of the IMF in our simulations.

In order to investigate internal trends that could be compared in a meaningful way with observations, we select all galaxies with intrinsic $u^* - r^* > 2$ and $\sigma_e > 150\,\mathrm{km\,s^{-1}}$ from each simulation, hereafter referred to as the 'Sigma150' sample (Fig. 4). Our conclusions regarding trends within these galaxies are as follows:

(i) High-σ_e galaxies exhibit strong radial IMF gradients, being either bottom or top heavy in the centre for LoM-50 and HiM-50 galaxies, respectively, and gradually transitioning to a Chabrier/Kroupa-like IMF beyond the half-light radius (Figs 2, 3, and 5). These trends result from the inside–out growth of galaxies, where the stars in central regions tend to have formed earlier

from interstellar gas with higher pressures than the stars in the outer regions (Fig. 6).

(ii) For both simulations, the IMF gradients result in an increase in the MLE toward the central regions, in qualitative agreement with recently observed MLE gradients in high-mass ETGs. While all high-σ_e galaxies in LoM-50 display negative MLE gradients, HiM-50 galaxies exhibit more diverse behaviour, with radial MLE gradients ranging from strongly negative to flat (Fig. 7). When measuring the IMF via the fraction of mass or light coming from low-mass dwarf stars, LoM-50 is consistent with observations of the centres of high-mass ETGs, while HiM-50 is in tension with the data (Fig. 8).

(iii) The difference in the radial MLE behaviour between LoM-50 and HiM-50 is likely a result of the strong dependence of the MLE on age in HiM-50, even at fixed IMF slope, as well as the larger scatter in birth ISM pressure within r_e in HiM-50 galaxies (Fig. 6).

(iv) All of our simulations produce negative stellar metallicity gradients, in agreement with observations. LoM-50 and Ref-50 produce weakly positive stellar [Mg/Fe] gradients. However, HiM-50 has enhanced [Mg/Fe] within r_e, causing [Mg/Fe] gradients to be much flatter, which may be more consistent with observed flat [Mg/Fe] profiles in high-mass ETGs (e.g. Mehlert et al. 2003; Parikh et al. 2018). While M/L gradients are flat in Ref-50, LoM-50 galaxies have strong negative M/L gradients and HiM-50 galaxies show a large diversity in M/L gradients, ranging from strongly positive to strongly negative (Fig. 9). Such gradients must be taken into account when making inferences on the IMF via dynamical masses.

(v) We find strong positive correlations between the local MLE and local stellar metallicity for both LoM-50 and HiM-50 galaxies, qualitatively consistent with observations (Fig. 10, top row). This is true when considering all galaxies simultaneously or for individual galaxies. Correlations between MLE and local metallicity can thus occur naturally even when the IMF is not governed by metallicity at all.

(vi) We find strong negative and positive correlations between the local MLE and local stellar [Mg/Fe] for LoM-50 and HiM-50, respectively, when considering all galaxies simultaneously (Fig. 10, middle row). This finding may aid in distinguishing between these two IMF variation scenarios with observations.

(vii) When considering all Sigma150 galaxies simultaneously, the local MLE shows a weak positive correlation with the local stellar age for LoM-50 (Fig. 10, bottom row). However, the local MLE shows no systematic correlation with local age for individual galaxies in either simulation, implying that the overall local MLE−age correlations seen for the whole Sigma150 population are a global, rather than a local, property, consistent with the strong positive global MLE−age relation reported in Paper II. It is thus important for studies of the spatially resolved IMF to remove global trends between the MLE and galaxy properties before making inferences on local ones.

We have investigated the redshift dependence of the IMF and global galaxy properties in our variable IMF simulations. Our results are as follows:

(i) For LoM-50, the MLE−σ_e relation has a higher normalization at $z = 2$ than at $z = 0.1$ due to the typically higher pressures at which stars form at high redshift. In contrast, HiM-50 produces a much lower normalization at $z = 2$ despite the time dependence of stellar birth ISM pressures resulting in more top-heavy IMFs at early times (Fig. 11). This lower normalization arises due to the age dependence of the MLE parameter for the HiM prescription (Fig. 12).

(ii) The dwarf-to-giant fraction increases weakly toward higher redshifts for high-σ_e galaxies in LoM-50, consistent with the observed evolution for quiescent galaxies (Fig. 13). HiM-50 is inconsistent with these observations.

(iii) The ionizing flux of star-forming galaxies in HiM-50 increases with SFR surface density due to shallower IMF slopes at high pressures, and shows little evolution. This trend is consistent with observed star-forming galaxies, but our IMF slopes may be too shallow relative to the high-redshift observations (Fig. 14).

(iv) We speculate that a model with a hybrid IMF, which incorporates both a shallow high-mass slope and a steep low-mass slope at high pressures, may be able to simultaneously reproduce the observed ionizing flux in star-forming galaxies as well as the MLE and dwarf-to-giant ratio in ETGs.

(v) At $z > 2$, the cosmic SFR density is higher and lower in LoM-50 and HiM-50, respectively, than in Ref-50. However, below $z \sim 1$, LoM-50 matches Ref-50 while HiM-50 lies above Ref-50. The peak of star formation is shifted toward lower redshift in HiM-50 (Fig. 15). This shift is likely caused by a combination of the decreased star formation law and burstier stellar feedback at high z in HiM-50, decreasing the SFR at high z and delaying the infall of cold gas onto galaxies.

The findings presented in this paper highlight the importance of being able to spatially resolve the galaxies in which the IMF is constrained. Indeed, radial IMF gradients can have significant implications for dynamical mass measurements used to constrain the IMF (e.g. Bernardi et al. 2018), as well as when comparing quantities measured within different apertures (see van Dokkum et al. 2017). We have also shown that correlations between the IMF and local galaxy properties can differ both qualitatively and quantitatively from global relations between the same quantities. Thus, studies that do spatially resolve the IMF should take care to avoid confusing global and local IMF scaling relations when combining results for different galaxies.

ACKNOWLEDGEMENTS

REFERENCES

Alton P. D., Smith R. J., Lucey J. R., 2017, MNRAS, 468, 1594
Alton P. D., Smith R. J., Lucey J. R., 2018, MNRAS, 478, 4464
Arnaud M., Rothenflug R., Boulade O., Vigroux L., Vangioni-Flam E., 1992, A&A, 254, 49
Astropy Collaboration, 2013, A&A, 558, A33
Barber C., Crain R. A., Schaye J., 2018a, MNRAS, 479, 5448
Barber C., Schaye J., Crain R. A., 2018b, MNRAS, 482, 2515
Barro G. et al., 2013, ApJ, 765, 104
Benítez-Llambay A., 2017, Astrophysics Source Code Library, record ascl:1712.003
Benítez-Llambay A., Navarro J. F., Frenk C. S., Ludlow A. D., 2018, MNRAS, 473, 1019
Bernardi M., Sheth R. K., Dominguez-Sanchez H., Fischer J. L., Chae K. H., Huertas-Company M., Shankar F., 2018, MNRAS, 477, 2560
Bezanson R., Van Dokkum P. G., Tal T., Marchesini D., Kriek M., Franx M., Coppi P., 2009, ApJ, 697, 1290
Booth C. M., Schaye J., 2009, MNRAS, 398, 53
Boroson T. A., Thompson I. B., 1991, AJ, 101, 111
Brough S., Proctor R., Forbes D. A., Couch W. J., Collins C. A., Burke D. J., Mann R. G., 2007, MNRAS, 378, 1507
Calzetti D., 2001, PASP, 113, 1449
Cappellari M. et al., 2011, MNRAS, 413, 813
Cappellari M. et al., 2013a, MNRAS, 432, 1709
Cappellari M. et al., 2013b, MNRAS, 432, 1862
Cardelli J., Clayton G., Mathis J., 1989, in Allamandola L., Tielens A., eds, IAU Symp. Vol. 135, Interstellar Dust. Kluwer, Dordrecht. p. 5
Chabrier G., 2003, ApJ, 586, 1
Charlot S., Fall S. M., 2000, ApJ, 539, 718
Clauwens B., Schaye J., Franx M., Bower R. G., 2018, MNRAS, 478, 3994
Conroy C., Gunn J. E., 2010, ApJ, 712, 833
Conroy C., van Dokkum P. G., 2012, ApJ, 760, 71
Conroy C., Gunn J. E., White M., 2009, ApJ, 699, 486
Crain R. A. et al., 2015, MNRAS, 450, 1937
Dalla Vecchia C., Schaye J., 2012, MNRAS, 426, 140
Davis T. A., McDermid R. M., 2017, MNRAS, 464, 453
Dolag K., Borgani S., Murante G., Springel V., 2009, MNRAS, 399, 497
Ferreras I., Weidner C., Vazdekis A., La Barbera F., 2015, MNRAS, 448, L82
Fischera J., Dopita M., 2005, ApJ, 619, 340
Fontanot F., De Lucia G., Xie L., Hirschmann M., Bruzual G., Charlot S., 2018, MNRAS, 475, 2467
Furlong M. et al., 2017, MNRAS, 465, 722
Greene J. E., Janish R., Ma C. P., McConnell N. J., Blakeslee J. P., Thomas J., Murphy J. D., 2015, ApJ, 807, 11
Gunawardhana M. L. P. et al., 2011, MNRAS, 415, 1647
Gustafsson B., Edvardsson B., Eriksson K., Jorgensen U. G., Nordlund A., Plez B., 2008, A&A, 486, 951
Haardt F., Madau P., 2001, in Neumann D. M., Tran J. T. V., eds, Clusters of Galaxies and the High Redshift Universe Observed in X-rays, Savoie, France. p. 64
Kewley L. J., Ellison S. L., 2008, ApJ, 681, 1183
Kuntschner H. et al., 2010, MNRAS, 408, 97
La Barbera F., Ferreras I., Vazdekis A., de la Rosa I. G., de Carvalho R. R., Trevisan M., Falcón-Barroso J., Ricciardelli E., 2013, MNRAS, 433, 3017
La Barbera F., Vazdekis A., Ferreras I., Pasquali A., Cappellari M., Martín-Navarro I., Schönebeck F., Falcón-Barroso J., 2016, MNRAS, 457, 1468
Lejeune T., Cuisinier F., Buser R., 1997, A&AS, 125, 229
Lejeune T., Cuisinier F., Buser R., 1998, A&AS, 130, 65
Maraston C., Strömbäck G., 2011, MNRAS, 418, 2785
Marigo P., Girardi L., 2007, A&A, 469, 239
Marigo P., Girardi L., Bressan A., Groenewegen M. A. T., Silva L., Granato G. L., 2008, A&A, 482, 883
Martín-Navarro I., 2016, MNRAS, 456, L104

Martín-Navarro I. et al., 2015a, ApJ, 798, L4

Martín-Navarro I., La Barbera F., Vazdekis A., Falcón-Barroso J., Ferreras I., 2015b, MNRAS, 447, 1033

Martín-Navarro I. et al., 2015c, ApJ, 806, L31

Martín-Navarro I., La Barbera F., Vazdekis A., Ferré-Mateu A., Trujillo I., Beasley M. A., 2015d, MNRAS, 451, 1081

McAlpine S. et al., 2016, Astron. Comput., 15, 72

McConnell N. J., Lu J. R., Mann A. W., 2016, ApJ, 821, 39

Mehlert D., Thomas D., Saglia R. P., Bender R., Wegner G., 2003, A&A, 407, 423

Nanayakkara T. et al., 2017, MNRAS, 468, 3071

Oldham L., Auger M., 2018a, MNRAS, 474, 4169

Oldham L. J., Auger M. W., 2018b, MNRAS, 476, 133

Oser L., Ostriker J. P., Naab T., Johansson P. H., Burkert A., 2010, ApJ, 725, 2312

Parikh T. et al., 2018, MNRAS, 477, 3954

Planck Collaboration, 2014, A&A, 571, A1

Portinari L., Chiosi C., Bressan A., 1997, A&A, 334, 38

Rosas-Guevara Y. M. et al., 2015, MNRAS, 454, 1038

Sarzi M., Spiniello C., La Barbera F., Krajnović D., van den Bosch R., 2018, MNRAS, 478, 4084

Schaye J., 2004, ApJ, 609, 667

Schaye J., Dalla Vecchia C., 2008, MNRAS, 383, 1210

Schaye J. et al., 2015, MNRAS, 446, 521

Shivaei I. et al., 2018, ApJ, 855, 13

Sonnenfeld A., Leauthaud A., Auger M. W., Gavazzi R., Treu T., More S., Komiyama Y., 2018, MNRAS, 481, 164

Spolaor M., Forbes D. A., Proctor R. N., Hau G. K., Brough S., 2008, MNRAS, 385, 675

Springel V., 2005, MNRAS, 364, 1105

Springel V., White S. D. M., Tormen G., Kauffmann G., 2001, MNRAS, 328, 726

Springel V., Di Matteo T., Hernquist L., 2005, MNRAS, 361, 776

Thomas D., Maraston C., Bender R., 2003, MNRAS, 339, 897

Thomas D., Maraston C., Johansson J., 2011, MNRAS, 412, 2183

Van Der Wel A. et al., 2012, ApJS, 203, 12

van Dokkum P., Conroy C., Villaume A., Brodie J., Romanowsky A., 2017, ApJ, 841, 23

van den Bosch R. C. E., Gebhardt K., Gültekin K., van de Ven G., van der Wel A., Walsh J. L., 2012, Nature, 491, 729

Vaughan S. P., Davies R. L., Ziel-niewski S., Houghton R. C., 2018a, MNRAS, 475, 1073

Vaughan S. P., Davies R. L., Zielniewski S., Houghton R. C. W., 2018b, MNRAS, 479, 2443

Villaume A., Conroy C., Johnson B., Rayner J., Mann A. W., van Dokkum P., 2017, ApJS, 230, 38

Weidner C., Ferreras I., Vazdekis A., Barbera F. L., 2013, MNRAS, 435, 2274

Westera P., Lejeune T., Buser R., Cuisinier F., A. G. B., 2002, A&A, 381, 524

Wiersma R. P. C., Schaye J., Smith B. D., 2009a, MNRAS, 393, 99

Wiersma R. P. C. R., Schaye J., Theuns T., Dalla Vecchia C., Tornatore L., 2009b, MNRAS, 399, 574

Zhang Z.-Y., Romano D., Ivison R. J., Papadopoulos P. P., Matteucci F., 2018, Nature, 558, 260

Zielniewski S., Houghton R. C., Thatte N., Davies R. L., Vaughan S. P., 2017, MNRAS, 465, 192

This paper has been typeset from a T$_E$X/L^{A}T$_E$X file prepared by the author.